IOPscience iopscience.iop.org

Home Search Collections Journals About Contact us My IOPscience

Ripple formation on silicon by medium energy ion bombardment

This article has been downloaded from IOPscience. Please scroll down to see the full text article.

2009 J. Phys.: Condens. Matter 21 224004

(http://iopscience.iop.org/0953-8984/21/22/224004)

View the table of contents for this issue, or go to the journal homepage for more

Download details:
IP Address: 129.252.86.83
The article was downloaded on 29/05/2010 at 19:57

Please note that terms and conditions apply.

IOP Publishing — Journal of Physics: Condensed Matter
J. Phys.: Condens. Matter **21** (2009) 224004 (22pp) doi:10.1088/0953-8984/21/22/224004

TOPICAL REVIEW

Ripple formation on silicon by medium energy ion bombardment

Tapas Kumar Chini[1], **Debi Prasad Datta and Satya Ranjan Bhattacharyya**

Saha Institute of Nuclear Physics, 1/AF Bidhannagar, Kolkata 700 064, India

E-mail: tapask.chini@saha.ac.in

Received 7 January 2009
Published 12 May 2009
Online at stacks.iop.org/JPhysCM/21/224004

Abstract
The formation of a self-organized nanoscale ripple pattern after off-normally incident ion bombardment on the surface of amorphous materials, or on semiconductors like silicon that are easily amorphized by ion bombardment, has attracted much attention in recent years from the point of view of both theory and applications. As the energy of the impinging ions increases from low to medium, i.e. several hundred eV to a few tens of keV, the ratio of amplitude to wavelength of the generated ripple pattern becomes so large that inter-peak shadowing of the incident ion flux takes place. Morphologically, the sinusoidal surface profile starts to become distorted after prolonged ion bombardment under such conditions. Structural and compositional modifications of the ripple morphology generated under shadowing conditions include the formation of a thicker amorphous layer with high incorporation of argon atoms in the form of nanometer sized bubbles around the middle part of the front slope of the ripple facing the ion beam, as compared to the rear slope. The present paper reviews recent developments in the experimental study of morphological, structural and compositional aspects of ripple patterns generated on a silicon surface after medium keV (30–120 keV) argon bombardment mainly at an angle of ion incidence of 60°.

Contents

1. Introduction 2
 1.1. Brief description of the theoretical works 3
 1.2. Shadowing effect 6
2. Experimental details 7
3. Morphological aspects of Ar ion induced surface ripples in Si 7
 3.1. Definitions of correlation functions, ripple parameters and correlation lengths: method of data analysis 7
 3.2. Ripple pattern coarsening for 60 keV Ar ion bombardment on Si at an angle of ion incidence of 60° 8
 3.3. Coarsening of surface ripples on Si by 30 keV Ar ion bombardment 11
 3.4. A brief comparison of the Si surface ripples obtained at 60 and 30 keV Ar ion bombardment with some recent experimental works 13
 3.5. Ion energy dependence of ripple wavelength 13
4. Compositional heterogeneity of medium energy Ar ion induced ripples in Si 14
5. Structural investigation of keV Ar ion induced surface ripples in Si 15
 5.1. Ripple structure versus luminescence property of silicon 16
6. Medium energy ion induced ripple evolution in binary semiconductors 17
 6.1. Ripple morphology on GaAs 17
7. Critical issues concerning the instrumentation and experimental conditions 18
 7.1. Need for an ion implanter 18
 7.2. Merits of broad beam based machines 19
 7.3. Sources of impurities 19

[1] Author to whom any correspondence should be addressed.

 © 2009 IOP Publishing Ltd Printed in the UK

8. Conclusion and outlook 20
Acknowledgments 21
References 21

1. Introduction

The development of new materials with tailor-made properties is currently a major field in science and technology. Surface and interface science is at the forefront of this development because surfaces and interfaces of materials dictate many of their important properties. Continuing progress in technological applications requires the engineering of interfaces with a wide range of physical, morphological or chemical properties. In this connection, heavy ion bombardment is thought to be a unique method for growth and modification of state-of-the-art material surface and interfaces [1]. The depth of the material surface that can be modified is crucially dependent on the energy of the ion beam. Accordingly, terminology has arisen to define the approximate ion energy ranges [1]. Ion energies below 1 eV are known as thermal, the energy range 1–500 eV is referred to as hyperthermal, 0.5–10 keV are low energy ions, 10–500 keV are medium energy ions and ions with energy beyond 500 keV are high energy ions.

The spectacular advent of surface characterization tools with an unprecedented resolution capability, ranging from atomic to nanometer length scales, has opened up newer and wider applications for ion beam modified surfaces. In particular, the spontaneous self-organization of surfaces into nanoscale patterns, such as one-dimensional periodic sinusoidal ripples [2–8] for off-normal ion beam incidence or two-dimensionally periodic dots [9–11] for a normally incident ion beam, has attracted much attention in recent years. Applications of such nanoscale patterns include the use of quantum dots for laser applications [9], magnetic quantum dots for information storage [12, 13] or periodically patterned glass surfaces as templates for organic material [14].

On the theoretical side, considerable insight into the mechanism of ion induced patterning has been achieved by continuum descriptions of ion bombarded amorphous surfaces [15–21] under two basic assumptions: (1) small variations of the surface modulations and (2) occurrence of ion beam sputtering (IBS) in the ion energy regime where the concept of the so-called linear collision cascade is valid. Assumption (1) refers to the small slope approximation, i.e. absence of shadowing, while assumption (2) depicts roughly the higher limit of the energy of the ion beam, which is typically about 100 keV [19] for theoretical models of ripple formation. For ripple generation using low keV ion beams with a low angle of ion incidence, inter-peak shadowing of the incident ion flux is not observed in general because the amplitude is much smaller than the wavelength of the ripples. Consequently, many aspects of the experimentally observed ripple morphology for low energy ion beam sputtered surfaces are in agreement with the theoretical predictions.

For medium energy ion bombardment, however, for the ripple morphology generated under 60 keV Ar → Si at an ion incidence angle of 60° [7], as the bombardment time

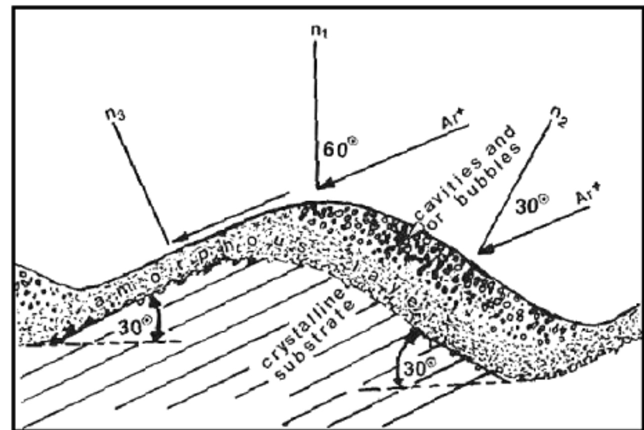

Figure 1. Schematic diagram of the microstructure of a medium energy Ar ion induced Si surface ripple obtained from TEM measurements. Reproduced with permission from [23]. Copyright 2003 by the American Physical Society.

increases after a critical value of the ratio of amplitude to wavelength [22], inter-peak shadowing of the incident ion flux distorts the sinusoidal ripple habit to a faceted one and the dynamical behavior of the ripple pattern could no longer be compared with the theoretical models. When the shadowing condition is reached the front slope of the ripples facing the ion beam will have more ions with an angle of incidence close to the local surface normal than the opposite face where the local angle of ion incidence is close to grazing, causing most of the ions to be reflected instead of being implanted. So a larger depth of the front slope will be affected both structurally and compositionally [23, 24] compared with the rear slopes, resulting in a thicker surface amorphous layer with the inclusion of high density Ar bubbles/cavities on the front slope facing the ion beam, as sketched in figure 1. Thus a number of issues remain to be clarified, especially for the ripple pattern observed with medium energy ion bombardment, such as the influence of shadowing or the effect of cavity/gas bubbles on the sinusoidally patterned surface profiles under long time bombardment. A recent simulation [25] shows that for technological applications such as nanowire fabrication, one should use a high keV oblique incidence ion beam that gives rise to a V-shaped ripple pattern. For such high energy induced corrugated patterns with high amplitude, the simulation did not consider the unavoidable effect of shadowing and compositional heterogeneity caused by non-uniform incorporation of implanting ions that may cause distortion of the desired profile.

Silicon was selected for our experimental study because it is amorphized at low ion fluence by bombardment with medium energy heavy ions such as argon. In addition, it can be considered as an ideal monoatomic solid for experimental studies in conjunction with the theoretical models which assume an amorphous monoatomic system. On the other hand, silicon has faced another challenge from the evolution of information technology. The need to increase operational speed in integrated circuits and advances in fiber-optic communication networks have promoted optical links as a substitute for electrical links. Silicon, which is an indirect

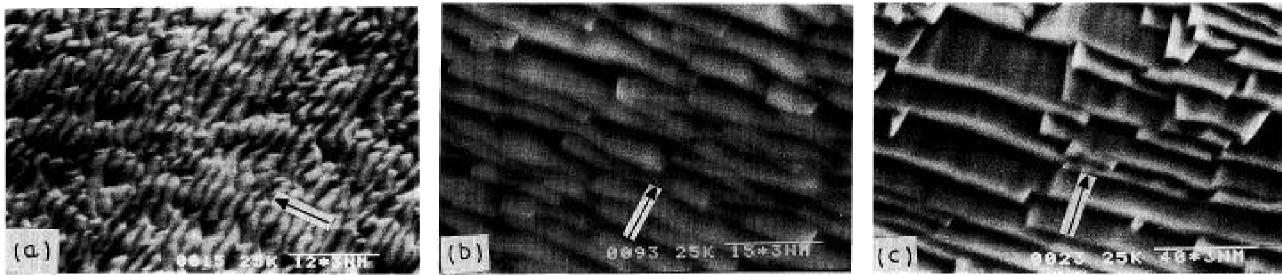

Figure 2. Electron micrograph of the corrugated terrace steps developed on a Si surface by 30 keV Ar^+ ions with a 58° angle of incidence at various doses: (a) dose $\simeq 1.26 \times 10^{19}$ ions cm^{-2}, magnified 2500×; (b) dose $\simeq 1.84 \times 10^{19}$ ions cm^{-2}, magnified 2000×; (c) dose $\simeq 8.4 \times 10^{19}$ ions cm^{-2}, magnified 750×. The arrows indicate the direction of ion incidence. Note that the size of the facets increases with dose. Reproduced with permission from [27]. Copyright 1991, the Japan Society of Applied Physics.

band gap semiconductor, has poor light emitting properties. Accordingly, conferring optical functionality on silicon has become a challenging research topic. Quite recently we have shown [26] that amorphous nanostructured Si mixed with high density Ar bubbles generated under off-normal Ar bombardment conditions can have favorable luminescence properties (similar to chemically synthesized porous silicon) which are not otherwise achievable in a well controlled manner for indirect bandgap materials like silicon. Consequently, not only is the top surface morphology of a ripple pattern controllable, but there is also the possibility of generating and controlling new types of nanostructured morphologies underneath surface ripples produced under medium energy heavy inert gas ion bombardment. This aspect has been scarcely explored in the area of ion beam modification of surfaces.

About two decades ago, just after the publication of the first theory [15] of ripple formation by ion bombardment, our group reported [27] the observation of ripple formation on a Si surface using a 30 keV Ar^+ beam delivered from a 50 kV laboratory scale isotope separator machine. The main results of this study are shown in the scanning electron microscope (SEM) images of figure 2. Although, the ripple orientation was in accordance with the theory [15] further study on the Si rippling process was not pursued at that time because of the unavailability of both sophisticated commercial surface probes like AFM and sound theories beyond that mentioned in [15]. However, after the publication of rigorous continuum models [16, 17] in the last decade many interesting features of ion beam sputter (IBS) morphology were predicted. These predictions had direct implications for the development of non-equilibrium phenomena in condensed matter physics and nanoscience research. Consequently, we and other groups involved in this field found renewed interest in the topic.

Section 1 reviews briefly the theoretical aspects, including the Bradley and Harper (BH) model, the Makeev, Cuerno, Barabási (MCB) model and the Garcia, Cuerno, Castro (GCC) model and also the concept of geometrical shadowing (section 1.2). Experimental details of the ripple data presented in this review are described in section 2. We then review our experimental results on the time evolution of ripple patterning on Si undergoing 60 keV Ar^+ bombardment at a 60° angle of incidence (section 3.2) and undergoing 30 keV Ar^+ bombardment (section 3.3). A comparison of the results obtained for these two bombardment energies is reviewed in section 3.4. Section 3.5 reviews the ion energy dependence of ripple wavelength. The compositional and structural modification of the silicon ripples is reviewed in sections 4 and 5. Considering the importance of GaAs as an electronic material, the salient features of medium energy Ar^+ induced rippling phenomena in GaAs is outlined in section 6. Relevant critical issues on the instrumentation and experimental conditions are discussed in section 7. Finally, we present a conclusion and outlook in section 8.

1.1. Brief description of the theoretical works

As detailed descriptions of the latest developments in the theoretical aspects of ion eroded surfaces will be given in this issue by renowned theoreticians, we will just present here the essential features of the different theoretical models. We will keep to a minimum the mathematical expressions of these theories, but they are absolutely necessary for understanding both the conceptual ideas and the implications of the experimental data presented in this review.

1.1.1. Bradley and Harper's model. Let us first sketch a general drawing of the ion bombardment induced ripple experiment (figure 3) with respect to which the continuum models are described. The length scale used in continuum models is much larger than the atomic scale. In addition, the solid surface is assumed to be a continuum of points, described by a surface height function $z = h(x, y, t)$ measured from laboratory coordinates whose x, y axes can be taken to be parallel to the initial flat surface and the z axis to be normal to the surface depicted in figure 3. The local coordinate system is defined by x', y', z'. The incoming beam is assumed to be aligned along the z' direction and makes an angle φ with the local surface normal and an angle θ with the surface normal of the initial flat surface of the laboratory coordinate system. They are related by the relation $\varphi = \theta + \frac{\partial h}{\partial x}$. While φ changes from point to point along the surface, θ remains fixed.

The first theoretical model of ion bombardment induced ripple formation on amorphous material was developed by Bradley and Harper (BH) [15] who basically employed Sigmund's theory [28] of sputtering as the starting point of

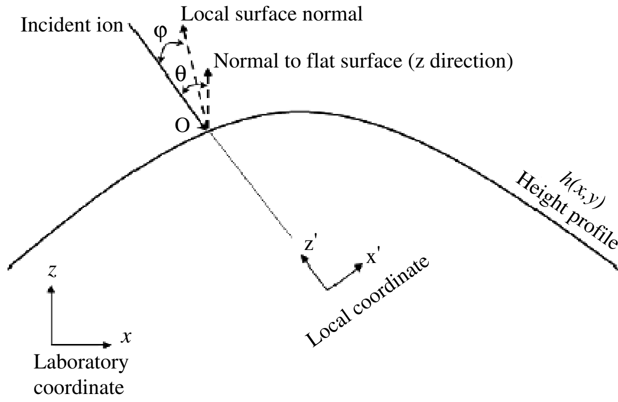

Figure 3. Sketch of the coordinate system for ion bombardment experiments.

their model. Sigmund's theory [28] of sputtering, which is valid for amorphous materials, assumes the effect of physical sputtering only. The rate at which the material is sputtered from a point O (see figure 3) of a surface is proportional to the energy deposited there by the random distribution of the incoming ions. The ejection of surface atoms from the generic point O of the interface is induced by the generation of recoils within the vicinity of the surface of the target of bombardment via transfer of kinetic energy from projectile to target atoms (being a purely elastic energy transfer process) without formation of any chemical compound between the projectile and target atoms. If $v_0(\theta) = \frac{f}{N}Y_0(\theta)\cos(\theta)$ is the rate of erosion of the unperturbed planar surface, with Y_0 being the sputtering yield at 0° angle of ion incidence (with respect to the uneroded initial flat surface), Sigmund's curvature dependent sputter erosion rate is given by

$$v(\theta, S) \cong \frac{f}{N}Y_0\left[\cos\theta + \Gamma_1(\theta)\frac{a}{S}\right]. \qquad (1)$$

Here, $\Gamma_1(\theta) = \frac{A}{B_1}\sin\theta - \frac{B_2}{2B_1}(1+\frac{A^2}{B_1})\cos\theta - \frac{AC}{B_1^2}(3+\frac{A^2}{B_1})\cos\theta$. A, $B_{1,2}$ and C are functions of θ and average depth of energy deposition (a) and their functional form is given in [15]. N is the number of atoms per unit volume in the amorphous solid and f is the ion flux.

Assuming a slowly modulating surface where the variation of height z or $h(x, y)$ is comparable with the average depth of energy deposition, a, and that the radius of curvature, S, at any surface point is much larger than a, BH derived a linear partial differential equation for a flat surface undergoing erosion following Sigmund's idea of curvature dependent sputtering while simultaneously undergoing surface relaxation toward flatness by surface diffusion. Such instability survives irrespective of the extent of the simultaneous relaxation due to surface diffusion processes. The resulting differential equation of BH for the change in height, relative to the average height, is

$$\frac{\partial h}{\partial t} = -v_0(\theta) + v_0'(\theta)\frac{\partial h}{\partial x} + \nu_x(\theta)\frac{\partial^2 h}{\partial x^2} + \nu_y(\theta)\frac{\partial^2 h}{\partial y^2} - D^T\nabla^4 h. \qquad (2)$$

The only surface smoothing process considered in the BH model is the thermally activated surface relaxation term $D^T\nabla^4 h$, introduced by Mullins [29] and Herring [30], with $D^T = \frac{2D\gamma\sigma}{N^2 k_B T}$ where D, γ, σ represent the surface self-diffusivity, the free energy per unit area and the number of atoms per unit area moving across the surface, respectively. k_B is Boltzmann's constant. $\nu_x(\theta)$ and $\nu_y(\theta)$ can change sign as the angle of incidence of the ion is varied. The sputtering yield, depending on the surface gradient and curvature terms $\nu_x(\theta) = \frac{fa}{N}\Gamma_1(\theta)$ and $\nu_y(\theta) = \frac{fa}{N}Y_0\Gamma_2(\theta)$, generates surface roughening.

According to BH, the curvature dependence of sputtering yield makes the surface unstable against the development of sinusoidal modulations. The linear partial differential equation (2) can be solved using Fourier methods and the balance between the unstable erosion terms $-|\nu_x|\frac{\partial^2 h}{\partial x^2}$ and $-|\nu_y|\frac{\partial^2 h}{\partial y^2}$ and the smoothing term $D^T\nabla^4 h$ generates sinusoidal ripples with a wavelength

$$l_i = 2\pi\frac{2D^T}{|\nu_i|} = 2\pi\left[\frac{2ND^T}{faY_0(\theta)|\Gamma(\theta)|}\right]^{\frac{1}{2}}. \qquad (3)$$

where i refers to the direction (x or y) along which the associated $|\nu_i|$ is the largest or $\Gamma(\theta)$ the smallest between $\Gamma_1(\theta)$ and $\Gamma_2(\theta)$. According to equation (3), the ripple orientation should be perpendicular to the beam direction (which is defined as the x direction of the surface) for angles of incidence less than a critical value θ_c, and parallel to the beam direction for angles close to grazing. The amplitude of each Fourier component of the surface morphology $h_k(t)$ with wavenumber k should grow or decay exponentially with a growth rate $r = -\nu_i k_i^2 - D^T k_i^4$ (assuming isotropic surface diffusion D^T for an amorphous surface). According to BH, the wavelength and orientation of the observed ripple pattern on the surface correspond to the value of $k_{x,y}$ for which the growth rate r is a maximum. So, the ripple wavelength, l_i, predicted by BH in equation (3) corresponds to the fastest growing spatial frequency k^* with $k^* = \frac{2\pi}{l_i}$, which should be time-independent as long as the curvature and range of slope remain sufficiently small.

The dependence of ripple wavelength on ion flux ($l \sim f^{-1/2}$), as explicitly expressed in equation (3), is strictly valid for small f values and the high T regime. Since $\nu_{x,y}$ do not depend on T, assuming $D^T \sim (1/T)\exp(-\Delta E/k_B T)$ where ΔE is the activation energy for surface diffusion, the dependence of ripple wavelength on temperature from equation (3) can be written as $l \sim (1/T^{1/2})\exp(-\Delta E/2k_B T)$. Also, assuming that the mean depth of energy deposition, lateral and longitudinal straggling are proportional to ion energy (E) and independent of flux (f), the BH predicted dependence of ripple wavelength on ion energy can be written as $l \sim E^{-1/2}$.

The BH theory predicts the ripple wavelength and orientation in agreement with numerous experimental studies. However, this theory cannot explain a number of experimental observations, such as the saturation of the ripple amplitude [31], the appearance of rotated ripples [5] and kinetic roughening [32, 33].

1.1.2. The Makeev, Cuerno and Barabási model. To remove some of the shortcomings of the BH model, Cuerno and Barabási (CB) [16] and more generally Makeev, Cuerno and Barabási (MCB) [19] extended the BH model by adding three terms to the expression (equation (2)) for the BH predicted height profile. (1) Slope dependent nonlinear terms of the form $\lambda_{i,j}(\nabla h)^2$. (2) Ion induced effective surface diffusion (ESD) [34] terms, like, $D^I_{ij}\nabla^4 h$ $(i, j = x$ or $y)$. Although the ion induced ESD term does not signify any mass transfer in the classical sense of diffusion, it plays the same role as thermal surface diffusion in the patterning of the surface under ion bombardment. ESD terms are generated by preferential erosion of the bombarded surface, i.e. certain parts of the surface are eroded faster than the other parts, depending upon the local surface morphology. If the system is viewed from a coordinate frame moving together with the average height of the surface, this preferential erosion appears as a reorganization of the surface, corresponding to a surface diffusion-like mechanism. (3) The uncorrelated white noise term $\eta(x, y, t)$ with zero average mimicking the local random fluctuation of the incident ion flux.

So, MCB obtained an anisotropic Kuramoto–Shivasinsky (AKS) type differential equation for the surface evolution as given below

$$\partial_t h = \nu_{i,j}\nabla^2 h - D^I_{i,j}\nabla^4 h + \frac{\lambda_{i,j}}{2}(\nabla h)^2 + \eta(x, y, t). \qquad (4)$$

Analytical solution of equation (4) is not possible due to the presence of nonlinear terms. The numerical integration of this AKS type equation by Park *et al* [20] demonstrated that the evolution of the surface with sputtering time can be classified into two regimes, one below t_c, designated as the linear regime, and the other beyond t_c, called the nonlinear regime, depending upon the sign of the product of coefficients of nonlinear terms λ_x and λ_y.

The crossover time t_c can be estimated from a comparison of the strengths of linear and nonlinear terms of equation (4) and follows the expression [20]

$$t_c \sim \frac{D^I}{\nu^2}\ln\frac{\nu}{\lambda}. \qquad (5)$$

Here, ν, λ and D^I refer to direction perpendicular to the ripple orientation. Below t_c, the MCB equation (4) is equivalent to the linear BH equation. Thus, keeping $\lambda = 0$ and $\eta = 0$ in the MCB equation, one obtains a similar expression for the ripple wavelength to that derived in the BH case, except that the numerator D^T of equation (3) will now be replaced by D^I, provided no thermal bias is active on the surface. Thus, a significant difference of the MCB model is that, without thermally activated surface relaxation, the ion induced ESD mechanism can give rise to a ripple pattern. However, in reality, even though the bombardment process starts with the sample at room temperature (RT), ion beam heating of the sample (in the absence of cooling arrangement as is the case in most of the experiments) is unavoidable for high flux and medium energy ions and, therefore, the sample temperature is increased. So, the diffusion terms in the MCB equation should consist of ion induced ESD terms plus thermally activated surface diffusion terms (the same as in the BH model), making the total surface diffusion coefficient $K = D^T + D^I$.

After a certain period of ion beam sputtering, beyond t_c, nonlinear effects become dominant. For $\lambda_x\lambda_y > 0$ the following results are predicted: The surface width w of the ion induced rippled surface stabilizes abruptly. Furthermore, the ripple pattern generated in the linear regime disappears and the ion sputtered surface exhibits kinetic roughening. In addition to the constant average erosion velocity $(-v_0)$ of the surface under ion sputtering (omitted from equation (4) and from the following discussion as it does not affect the surface morphology), a contribution to the erosion velocity comes from the nonlinear terms. The effect of nonlinearity on the ion sputtered surface evolution for the case of $\lambda_x\lambda_y < 0$ is quite different from that of $\lambda_x\lambda_y > 0$ case. The nonlinear behavior in this case can be manifested, after t_c, either by showing a kinetic roughening behavior or by suddenly developing a new ripple morphology in which the patterns are stable and rotated at an angle θ with respect to the x direction. However, no definite experimental observation exists that favors these predictions. In this regime, the surface can be described by the scaling exponents as explained in [17]. The asymptotic scaling of the KS equation is exactly known in 1+1 dimensions both analytically [35] and numerically [16] to approach that of Kardar–Parisi–Zhang equation [36].

1.1.3. García, Castro and Cuerno model. Quite recently a ‘hydrodynamic’ model [37] based formalism [38] developed by García *et al* [21] (here after called the GCC model) has been introduced as a suitable generalization of continuum description of ripples produced under erosion by ion beam sputtering (IBS) of amorphous targets at off-normal incidence. The essential feature of the GCC model is that in the process of surface evolution caused by IBS, the surface atoms are not only sputtered away but may also join the current of surface adatoms that are available to other relaxation mechanisms, such as surface diffusion, before being incorporating back into the solid bulk. Thus, the main difference between the former models [15, 16, 20] and the GCC model [21] is that, in the latter, a fraction (1-ϕ) of eroded material is allowed to redeposit locally. Besides, in addition of the time evolution of the height of the bombarded surface, $h(x, y, t)$, there is an implicit viscous flow [39] in the amorphized layer through the evolution of another coupled field $H(x, y, t)$, i.e. the thickness of the mobile surface adatoms layer. More importantly, apart from the nonlinear term, $\lambda^{(1)}_i$ of the earlier model [16] additional nonlinear terms also appear in the GCC model. Following GCC [21], the surface height evolution $h(x, y, t)$ of a sputter eroded amorphous material can be described by

$$\partial_t h = \sum_{i=x,y}\{-\nu_i\partial_i^2 h + \lambda^{(1)}_i(\partial_i h)^2\} + \sum_{i,j=x,y}\{-K_{ij}\partial_i^2\partial_j^2 h + \lambda^{(2)}_{ij}\partial_i^2(\partial_j h)^2\}. \qquad (6)$$

For simplicity, the zeroth and first order terms as well as the terms that are not responsible for pattern formation itself are omitted from equation (6) as has been done for equation (4). Also, ν_i and K_{ij} carry the same meaning of sputter erosion and

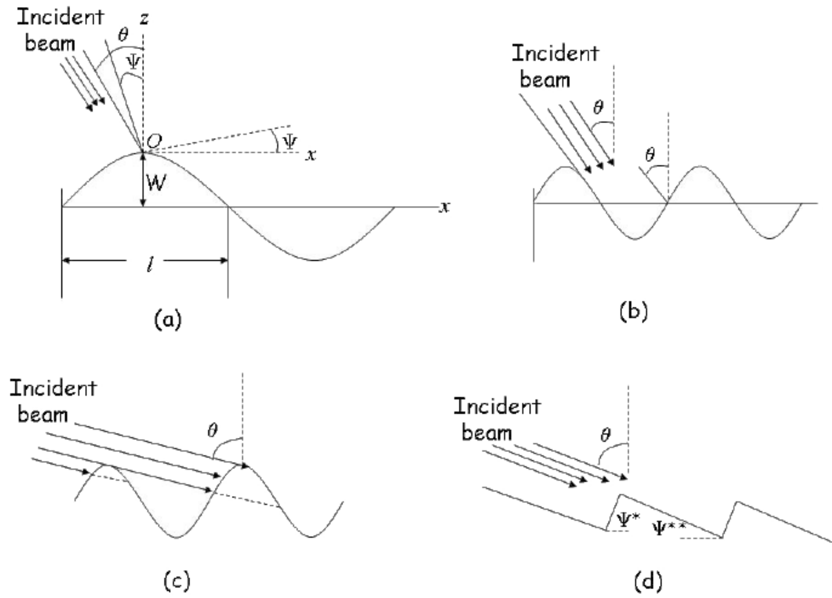

Figure 4. Illustration of geometry of ion bombardment on a sinusoidal profile. (a) The total surface is exposed to the ion beam. (b) Limiting condition for W/l for a given θ beyond which shadowing occurs. The incident ion beam is parallel to the back slope of the ripple pattern here. (c) The shadowing condition is exceeded, the ion flux can access only part of the ripple peaks and planarization occurs to initiate faceting. (d) Faceting is fully developed.

surface diffusion, respectively, as in the MCB model. However, the relaxation term K_{ij} and the nonlinear terms $\lambda_i^{(1)}$ and $\lambda_{ij}^{(2)}$ now depend on the redeposition parameter (ϕ), the angle of ion incidence (θ), the thermal diffusion (D^T) and a nonzero average fraction of mobile atoms (R_{eq}) that also contribute to smoothing. The various features of pattern dynamics such as the amplitude saturation, wavelength coarsening or appearance of rotated ripples or kinetic roughening etc crucially depend on the relative strength of the two nonlinear terms $\lambda_i^{(1)}$ and $\lambda_{ij}^{(2)}$.

1.2. Shadowing effect

Under off-normal ion incidence on a surface, the BH model or the linear version of the MCB model predict an exponential increase in amplitude of ripples with sputtering time. The development of surface slope due to the exponential increase in ripple amplitude can result, apart from the initiation of nonlinear effects, in a situation where the ion beam can be hampered by the preceding ripple peak and impinge on the upstream face of a ripple. This phenomenon, called the shadowing effect, becomes a factor of utmost importance in determining the evolution of ripple patterns when the angle of ion incidence is close to grazing or even at lower angle of ion incidence in the case of the relatively high amplitude ripple pattern evolution induced by medium energy ion bombardment. The effect of shadowing on the evolution of the ripple pattern can be understood from the geometrical argument introduced by Carter [22]. A schematic diagram illustrating Carter's argument is presented in figure 4.

In Carter's model, any fluctuation in regular sinusoidal ripple patterns with the wavevector aligned parallel to the projection of the ion beam on to the surface is ignored. Therefore, only a two-dimensional section in the xOz plane through the surface can be considered, as shown in figure 4(a). This surface profile can be described by $h = W\cos(2\pi x/l)$ where W is the ripple amplitude and l is the ripple wavelength. The ion beam impinges on the surface at an angle θ to the normal to the mean surface plane (the Oz axis). Over an incremental surface length ds, at the point O on the surface, the gradient of the surface slope is given by $\tan\Psi = \partial h/\partial x$. It is clearly visible that Ψ is also the angle between the local surface normal and the Oz axis. As the ratio between the ripple amplitude and ripple wavelength, W:l, increases, the maximum gradient of the sinusoidal ripple pattern $2\pi W/l$ becomes too large and, as a consequence, the local angle of incidence of the ion beam $(\theta - \Psi)$ decreases. Finally, a limiting condition is reached when the incident ion beam is parallel to the back slope of the ripple pattern, as shown in figure 4(b). For any further increment in the W:l ratio, part of the upstream face of the ripples is 'blocked' or 'shadowed' from the incident ion beam by the preceding peak in the waveform, as shown in figure 4(c). The limiting value of the ratio W:l for shadowing not to occur is given by

$$\tan\left(\frac{\pi}{2} - \theta\right) \geqslant \frac{2\pi W}{l} \tag{7}$$

which places an upper limit on the ratio W:l for any angle of ion incidence θ. If this ratio is exceeded then the valleys will not be eroded but the ripple peaks will be planarized as illustrated in figure 4(c). Although the dynamics of the subsequent changes in surface morphology is difficult to describe theoretically, it is reasonable to expect that a transformation to a sawtooth-like waveform will gradually evolve for prolonged ion sputtering, as shown in figure 4(d), with facets tilted at angles Ψ^* and Ψ^{**} with respect to the horizontal direction.

2. Experimental details

Ion bombardment of Si targets (p-type Si(001) single crystal wafer) was undertaken with a 200 kV high current ion implanter (Danfysik A/S, Denmark) which is described in detail elsewhere [40]. This medium energy implanter is capable of producing isotopically pure beams of almost all elements in the periodic table with beam currents varying from a few μA to 3–4 mA depending on the ion species. Si samples were irradiated in the implantation chamber (having a base vacuum in the range of 10^{-7} mbar) by a focused (with typical beam spot size of 1.5 and 2.5 mm) $^{40}Ar^{+}$ beam at a 60° angle of ion incidence (and in some case 70°) with respect to the surface normal of the samples. With a magnetic x–y sweeping system the focused beam was scanned over the sample to maintain homogeneous irradiation. The magnetic beam sweeping system of our implanter uses scan frequencies of 0.51 and 5.3 Hz along the horizontal and vertical directions to maintain beam homogeneity on the irradiated area of the sample. The scanned area could be varied from 5 mm × 5 mm to 25 mm × 25 mm. The beam flux in the present experiment was varied in the range 15–200 μA cm^{-2} and the maximum ion fluence varied up to $\sim 3.0 \times 10^{19}$ ions cm^{-2} covering a sufficiently long bombardment time of more than 8 h (for a typical flux of 175 μA cm^{-2}). To check the influence of beam scanning, several samples were irradiated without beam scanning where the flux was around 140 μA cm^{-2}.

Morphological characterization of the ion beam sputtered surface was performed *ex situ* by atomic force microscopy (AFM) using either an AutoProbe CP model (Park Scientific Instruments) or a NanoScope IV model (Veeco Analytical). In all the AFM studies AFMs were operated in contact mode using a Si_3N_4 tip of radius 10 nm and a contact force of 4–8 nN. The compositional analysis of the argon bombarded silicon surface was carried out using energy dispersive x-ray spectrometry (EDS) (EDAX Inc.) fitted in a field emission gun (FEG) based scanning electron microscope (SEM) (Quanta 200F, FEI Co). The crystalline structure of the selected sample was characterized by cross-sectional transmission electron microscopy (XTEM) using either a Philips CM300 TEM operating at 300 kV or a JEM-2000EX (JEOL) TEM operating at 200 kV. The specimens for XTEM were prepared using Gatan (USA) instruments for TEM sample preparation with the final thinning by a standard ion milling process.

3. Morphological aspects of Ar ion induced surface ripples in Si

Study of the evolution of ripple morphology with irradiation time is basically performed through the variation of two parameters, the ripple wavelength l (related to the ripple lateral dimension) and the surface roughness W (related to the ripple vertical dimension, i.e. ripple amplitude). Different models predict different behaviors of l with sputtering/irradiation time or ion fluence; for example, some models imply that l increases with sputtering time, meaning the pattern coarsens with time. Consequently, the experimental investigation of the evolution of ripple pattern with time is extremely important as the existence or non-existence of ripple coarsening could be a key test for the validity of the continuum models. In fact, ripple coarsening is not predicted by the seminal BH theory [15] or some of its nonlinear extensions [16]. In contrast, it is predicted by more recent theories [21]. Thus, the analysis of ripple coarsening becomes a relevant issue. The coarsening process is typically reflected in a power law dependence such as $l \sim t^{\gamma}$, where t is bombardment time (fluence) and γ is a coarsening exponent. The behavior of important statistical parameters, namely lateral correlation length and system correlation length, are also discussed in the context of time evolution of periodic patterned morphology [41]. These correlation lengths are intimately connected with the concepts of the height–height correlation function and auto-correlation function. In fact for quantitative analysis of ripple parameters (namely l and W) one often needs to use these statistical parameters. In section 3.1 we will define the concepts of correlation functions, different correlation lengths and the method of extracting ripple parameters from AFM image analysis.

3.1. Definitions of correlation functions, ripple parameters and correlation lengths: method of data analysis

Surface images acquired by AFM are digital images in which the image lattice is a two-dimensional array of $N \times N$ points giving the surface height h_{ij} ($i, j = 1$–N) at every point. The dimension of the image is $L = N\Delta$ where Δ is the step length of the AFM. The statistical parameters characterizing the surface can be estimated from the two-dimensional matrix of surface heights by a summation over the points instead of an integration. The mean or average height $\bar{h}$ and RMS roughness w is obtained from the matrix of surface point according to the relation given below,

$$\bar{h} = \frac{1}{N^2} \sum_{i=1}^{N} \sum_{j=1}^{N} h_j. \tag{8}$$

$$w^2 = \frac{1}{N^2} \sum_{i=1}^{N} \sum_{j=1}^{N} [h_j - \bar{h}]. \tag{9}$$

While the RMS roughness gives the average behavior of an individual point on the surface, the correlation among the heights of any two arbitrary points is quantified through the auto-correlation function $R(\rho)$ or the height–height correlation function $G(\rho)$ of the surface defined as [41]

$$R(\rho) = \frac{1}{(N-p)(N-q)} \times \sum_{l=1}^{N-p} \sum_{n=1}^{N-q} [\{h(p+n, l+q) - \bar{h}\}\{h(n,l) - \bar{h}\}]. \tag{10}$$

$$G(\rho) = \frac{1}{(N-p)(N-q)} \times \sum_{l=1}^{N-p} \sum_{n=1}^{N-q} [h(p+n, l+q) - h(n,l)]^2. \tag{11}$$

The above mentioned correlation functions have been defined for an anisotropic surface as is the case for a rippled surface.

The summation runs over the pairs of surface points p, q, and ρ denotes the spatial separation between the two points on the surface. The number of pairs p and q in two directions is kept much below N to ensure reasonable statistical averages. In case of patterned surfaces with one-dimensional periodic ripples or two-dimensional periodic dots or mounds, the periodicity of the surface is reflected through the oscillations in the correlation functions $R(\rho)$ or $G(\rho)$. It is known, however, that the oscillations in $G(\rho)$ or $R(\rho)$ can be observed even for a rough surface morphology due to sampling induced hidden cycles arising out of the correlation among the surface points [41]. For this reason, it is necessary to determine the periodicity of surface patterns from an average $G(\rho)$ or $R(\rho)$ taken over a large number of images. In our analysis, we found that four to six images from each sample were sufficient to give statistically reliable data to obtain $G(\rho)$. One usually uses $G(\rho)$ instead of $R(\rho)$ to study the properties of the random rough surfaces.

In the experimental studies of this review, the height–height correlation functions (also called height difference correlation functions), determined from the AFM images, are one-dimensional functions calculated along the fast scan direction on the images (designated as the x direction) and the other direction is averaged out. In this case $G(\rho)$ becomes

$$G(\rho) = \frac{1}{N(N-p)} \sum_{q=1}^{N} \sum_{n=1}^{N-p} [h(p+n,q) - h(n,q)]^2. \quad (12)$$

The height–height correlation function and the auto-correlation function are related as

$$G(\rho) = 2w^2[1 - R(\rho)]. \quad (13)$$

For a random rough surface the height–height correlation function has the form [41]

$$\begin{aligned} G(\rho) &\sim \rho^{2\epsilon} \qquad \text{for } \rho \ll \xi, \\ &\sim 2w^2 \qquad \text{for } \rho \gg \xi. \end{aligned} \quad (14)$$

The growth exponent ϵ for the surface can be determined from a linear fit to the log–log plot of $G(\rho)$ versus ρ.

According to the scheme for the analysis of periodically patterned morphology developed by Kim *et al* [42] we define the surface roughness amplitude W (the same as the ripple amplitude) as the value of $G^{\frac{1}{2}}(\rho)$ at the first local maximum, $W = G^{\frac{1}{2}}(d/2)$, where the characteristic in-plane length scale d is the position of ρ at the first local minimum of $G^{\frac{1}{2}}(\rho)$. This definition of roughness amplitude is preferred over the large ρ limit of $G^{\frac{1}{2}}(\rho)$ because AFM data can be affected by artifacts at large length scales. The spatial periodicity or wavelength l of the ripple patterns is found from the average peak to peak separation of the oscillations in the plot of $G^{\frac{1}{2}}(\rho)$ versus ρ [7].

The lateral correlation length ξ is defined as the value of ρ over which the auto-correlation function drops down to $1/e$ of its value at $\rho = 0$. The lateral correlation length ξ defines a representative lateral dimension on the surface. If the distance between two surface points is within ξ, the heights at these two points can be considered as correlated. If the distance of separation is much larger than ξ, the heights at these two point are independent of each other. For a periodically varying surface the auto-correlation and height correlation functions will vary periodically beyond ξ, reflecting the periodic nature of the surface. Even when the surface height is a superposition of a random height field and a periodic field of very small amplitude, the periodic correlation from the periodic field will dominate $R(\rho)$ at large length scales ($\rho \gg \xi$).

In case of a periodically varying surface that exhibits wavelength selection, i.e. average pattern separation l, the regularity in the distribution of the patterns across the surface can be characterized by another correlation length, called the system correlation length ζ [41]. When the surface patterns are regularly arranged over a surface area of lateral dimension much higher than the length scale of pattern separation, the system correlation length ζ is much greater than l. On the other hand, ζ is comparable to or less than l when patterns are confined within a surface area comparable to l. In other words, how randomly the patterned features are distributed over a surface can be represented by the system correlation length ζ. So, in the presence of periodic features, when $\zeta \gg l$, $G(\rho)$ and $R(\rho)$ exhibit regular periodic oscillations at a length scale $\rho \gg \xi$. However, when ζ falls below l, the oscillations become irregular, resulting in a random distribution of pattern features and $G(\rho)$ approaches the form of equation (14). As a quantitative expression, the following form of the height–height correlation function is proposed [43] for a mounded surface

$$\begin{aligned} G(\rho) &= 2w^2\left[1 - \mathrm{e}^{-(\frac{\rho}{\xi})^{2\alpha}} \cos\left(\frac{2\pi\rho}{l}\right)\right] \\ &\qquad \text{for } 1+1 \text{ dimension}, \\ &= 2w^2\left[1 - \mathrm{e}^{-(\frac{r}{\xi})^{2\alpha}} J_0\left(\frac{2\pi\rho}{l}\right)\right] \\ &\qquad \text{for } 2+1 \text{ dimension}, \end{aligned} \quad (15)$$

where $J_0(\rho)$ is the zeroth order Bessel function. If the ratio $\zeta{:}l > 1$, $G(\rho)$ shows an oscillatory behavior. Experimentally, the system correlation length can be estimated by a fit of $G(\rho)$ determined from AFM images (to be discussed in section 3.2) to equation (15).

3.2. Ripple pattern coarsening for 60 keV Ar ion bombardment on Si at an angle of ion incidence of 60°

The morphological evolution [7] of the bombarded Si surface (for an ion flux of 175 μA cm^{-2}) with sputtering time can be followed from representative AFM images at increasing sputtering times presented in figure 5.

A representative quasiperiodic ripple pattern from an early time morphology is presented in figure 5(a) for a sputtering time of 540 s. As the sputtering proceeds, the spatial periodicity or wavelength of the ripple morphology increases and the regular ripple pattern starts to be distorted, as shown in the AFM image of figure 5(b) for a sputtering time of 8160 s. If the sputtering is continued, the morphology, which looks more similar to a faceted ripple pattern as displayed in figures 5(c) and (d), remains stable for long time sputtering up to 30 300 s. A representative height profile of the ripple patterns taken along the line shown on the AFM images is displayed below

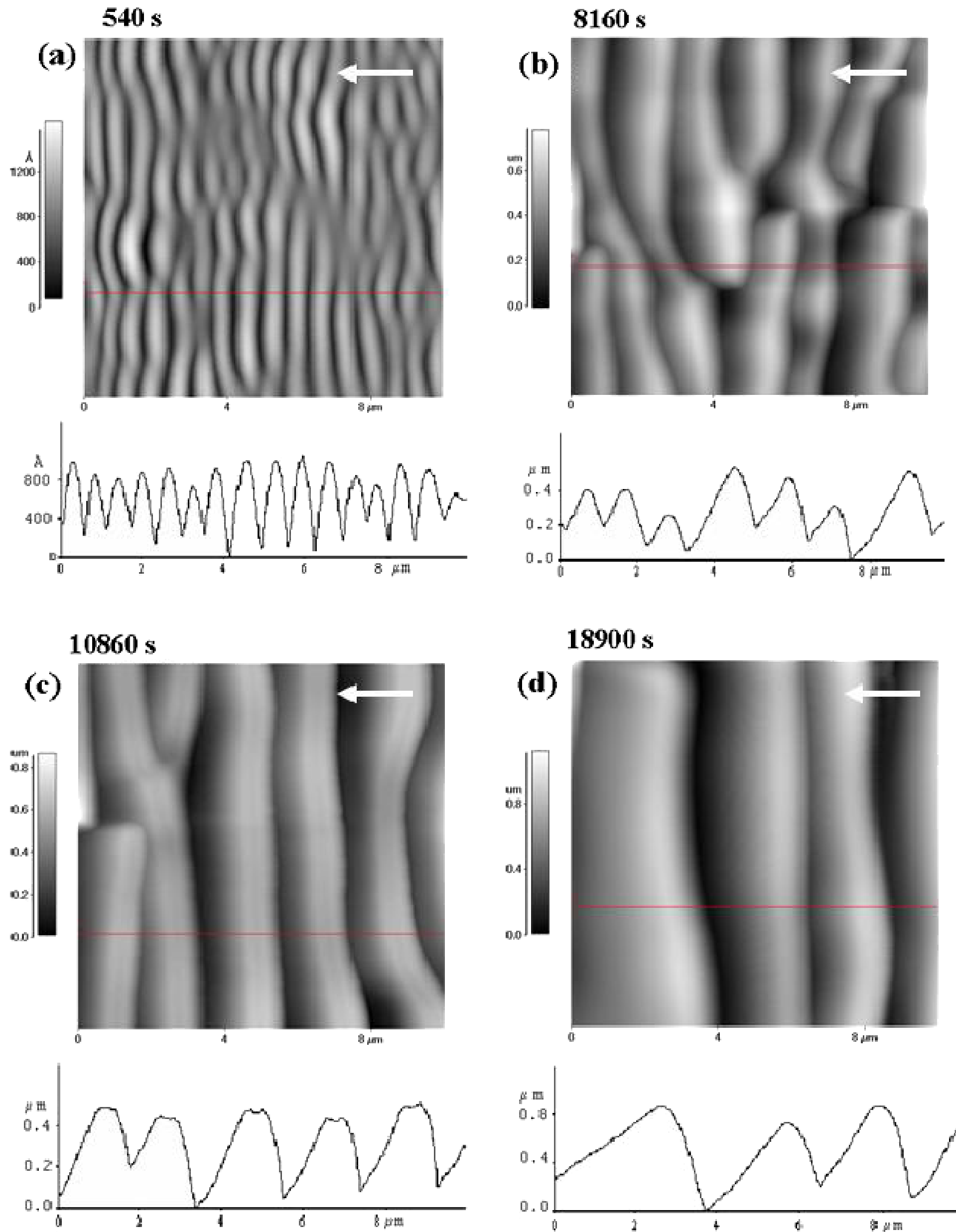

Figure 5. AFM images of Si surfaces at increasing bombardment times at a fixed flux of 175 μA cm^{-2}. The white arrow head indicates the beam direction.

each image in figure 5. Close inspection of the line profiles reveals that the habit of the surface patterns changes from sinusoidal (figure 5(a)) to triangular (figure 5(b)) and finally sawtooth-like (figure 5(d)) as a function of sputtering time. Similar transformation under oblique ion incidence has also been observed by other groups [2, 44, 45]. In all these stages of ripple pattern evolution, orientation of the ripples remains perpendicular to the projection of ion beam flux on the surface as indicated by the arrows over the AFM images in figures 5(a)–(d).

The roughness amplitude W and ripple wavelength l are plotted [7] as functions of sputtering time t in figure 6(a). W shows a power law behavior $W \sim t^{\beta}$ together with the time scaling behavior of the ripple wavelength $l \sim t^{\gamma}$ for the ion flux of 175 μA cm^{-2}. Figure 6(a) shows that the wavelength of the ripple pattern varies from 700 to 3500 nm while the roughness amplitude varies from 30 to 500 nm. With respect to ripple pattern evolution, we can identify three time regimes from figure 6(a). (1) Early time regime where the ripple wavelength l remains almost constant in the sputtering time region ∼440–750 s (a fluence range ∼4.0 × 10^{17}–8.0 × 10^{17} ions cm^{-2}). (2) Intermediate time regime that extends from ∼800 to ∼6000 s. The growth exponent $\beta = 0.76$ covers both the early and intermediate time regimes, whereas the exponent $\gamma = 0.64$ covers the intermediate time regime. (3) The late time regime spanning from ∼6000 to ∼30 300 s. The crossover values of β and γ fall into this regime.

In table 1, we report the system correlation length ζ and the ratio ζ:l with increasing sputtering time assuming that the one-dimensional height–height correlation function $G(r)$ has

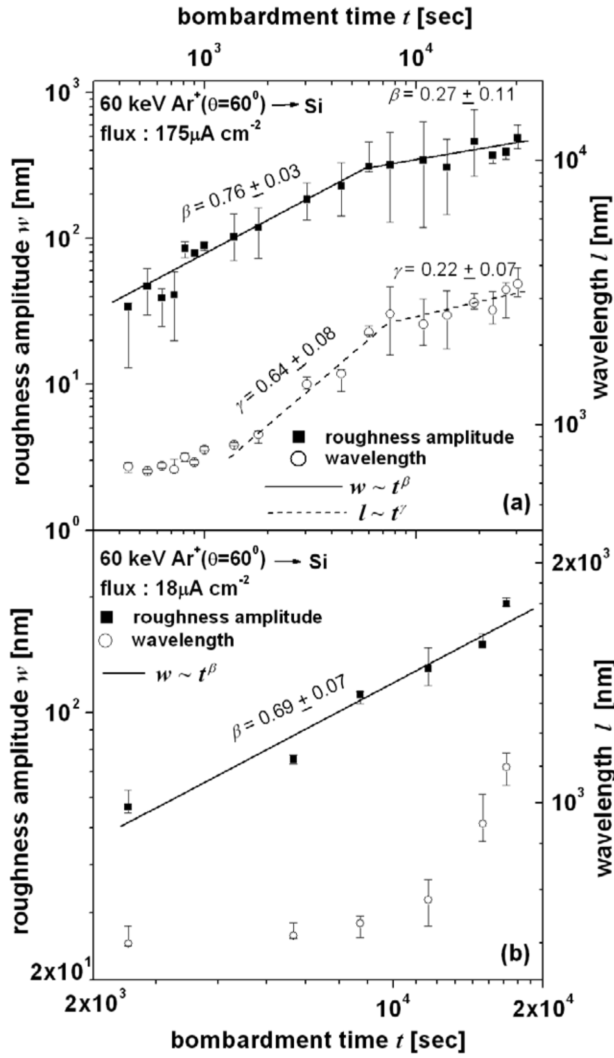

Figure 6. The ripple wavelength l and the surface roughness amplitude W as a function of bombardment time. Ion flux (a) 175 μA cm^{-2} and (b) = 18 μA cm^{-2}.

the form described in equation (15) in section 3.1. The lateral correlation lengths in the direction perpendicular to the ripple patterns (the x direction parallel to the projection of the ion beam onto the surface) and in the direction parallel to the ripples (the y direction), ξ_x and ξ_y, have also been determined from the AFM images according to the method described [41]. These correlation lengths are also shown in table 1. It can be seen from the table that, for an incident ion flux of 175 μA cm^{-2}, the ζ:l ratio increases from 1.48 at a sputtering time of 540 s to 1.53 at a sputtering time of 900 s, indicating more regular organization of ripple pattern on the surface with increasing sputtering time. This is in excellent agreement with our observation from the AFM images that the quasiperiodic ripple patterns at low sputtering time around 540 s (shown in figure 5(a)) become well formed at a sputtering time of 900 s. The ζ:l ratio at a sputtering time of 10 860 s is seen to decrease to a significantly smaller value, 0.7. This sputtering time corresponds to the late regime of ripple evolution where the ripple pattern becomes distorted and a regular wavelength of the ripple patterns cannot be defined. The distortion of regular

Table 1. The lateral correlation lengths and system correlation lengths for 60 keV $^{40}Ar^+$ bombardment induced ripple patterns on Si, obtained from a fit of equations (15) to $G(r)$ calculated from AFM images.

Ion flux (μA cm^{-2})	Ion fluence (ions cm^{-2})	Time (s)	ξ_x (nm)	ξ_y (nm)	ζ (nm)	ζ:l
	5.6×10^{17}	540	129	1106	989	1.48
175	1×10^{18}	900	152	1058	1108	1.53
	1.2×10^{19}	10 860	530	3644	1688	0.70

patterns is found to be correctly reflected by a ζ:l ratio of less than 1. In the x direction, ξ_x is a function of ζ and l [41]. The fact that ξ_y remains much greater than ξ_x for both incident ion fluxes shows much less local roughness of the surface along the y direction compared to the x direction.

For the angle of incidence used in the present experimental condition ($\theta = 60°$), the maximum angle (Ψ) of the slope of the ripples should be ($\pi/2$–$\pi/3$) = 30° or $W/l \leqslant 0.09$ to avoid shadowing as described in section 1.2. Beyond 800 s, throughout the intermediate and late stage of ripple dynamics, the W:l ratio remains in the range 0.1–0.16. Therefore, the surface dynamics at intermediate and late stages including the power law variation of the ripple amplitude and wavelength as well as the transition from ripple patterns to faceted morphology, can be thought to be dominated by shadowing effects. Presumably, the shadowing transition triggers a nonlinear process as one goes from the early time to intermediate time regime (figure 6(a)) and the sputtering time $t = 800$ s corresponding to the onset of increase in ripple wavelength l can be taken as a rough measure of t_c separating the linear and nonlinear regimes [20]. From reference [20], it is also seen that

$$t_c \sim \frac{1}{f}, \tag{16}$$

where f is the ion flux.

To study the dependence of t_c on ion flux f we have monitored the surface evolution at an ion flux ten times smaller than 175 μA cm^{-2}, namely at around 18 μA cm^{-2}, keeping other experimental parameters constant. The result is shown in figure 6(b). From comparison of figures 6(a) and (b) one can see that the time for the onset of nonlinearity has shifted by a factor of 10. Although the critical time t_c of shadowing transition increases at lower flux, the critical fluence (ϕ_c) corresponding to the critical time (t_c) remains more or less the same because ion fluence = flux × time. We estimate the critical fluence for the shadowing transition or the onset of increase in ripple wavelength from the present data of figure 6 to be ~8–9 × 10^{17} ions cm^{-2}. Therefore, we show that there exists a critical fluence for the shadowing transition to occur for ion induced ripple evolution. This transition can be achieved for short (long) sputtering times by using high (low) ion flux values. Other effects associated with shadowing may influence the late stages of dynamic evolution of the surface. These effects include redeposition of sputtered atomic species as well as the scattered ion flux, which can locally enhance the incident ion flux [2].

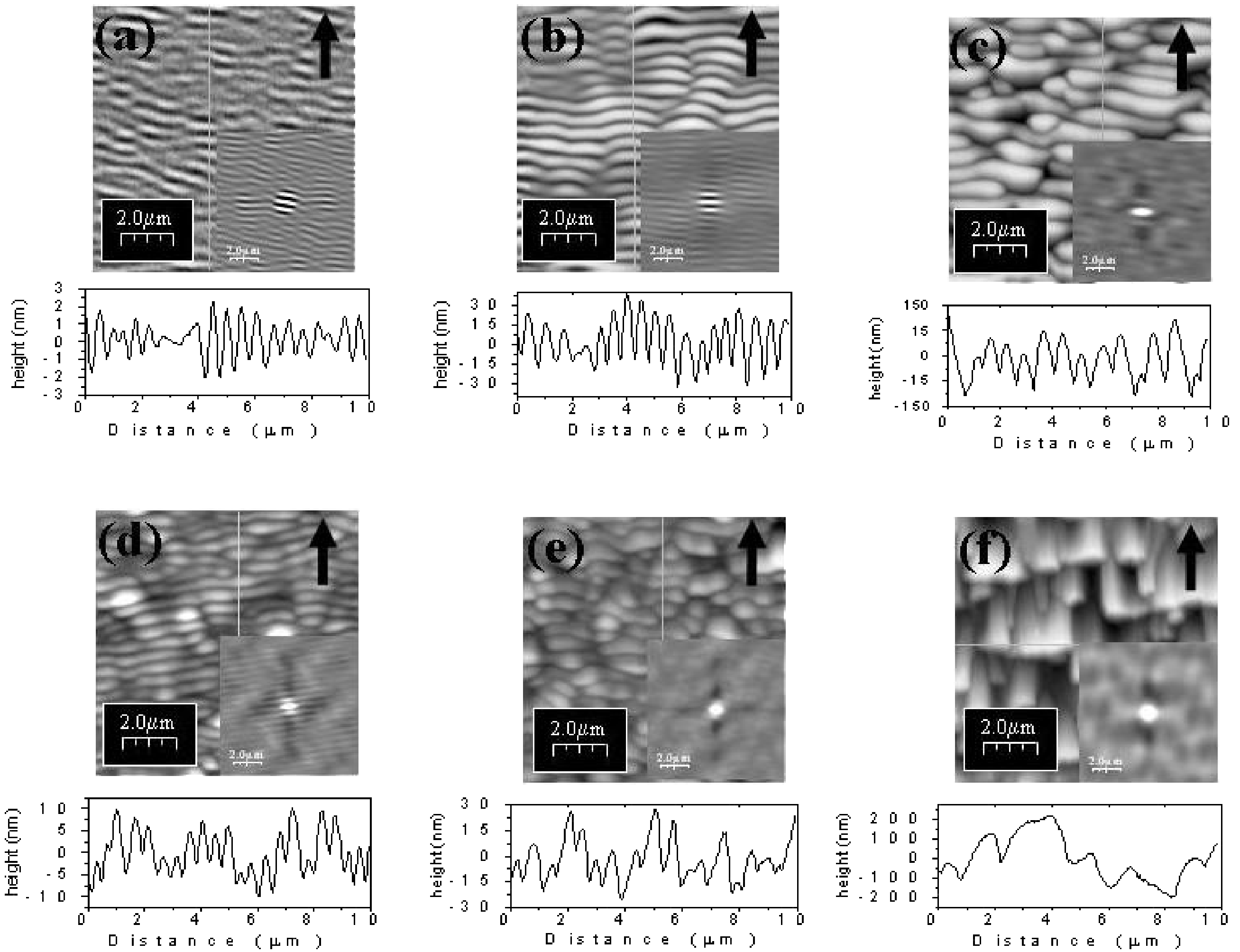

Figure 7. AFM images of Si surfaces sputtered with Ar^+ for different sputtering times: (a) 5700 s, (b) 10700 s, (c) 26600 s at $E_{\mathrm{ion}} = 30$ keV, $\theta = 60°$ (upper panel) and (d) 7500 s, (e) 11300 s and (f) 28200 s at 70° (lower panel). The height profiles shown under each of the AFM images are taken along the line indicated in the images. The black arrow head indicates the beam direction.

In the limit of large times ($t \gg t_c$) and large length scales ($l \gg l_c$), for $\lambda_x\lambda_y > 0$ (which is the case for the present results), the continuum theory of MCB predicts kinetic roughening of the ion bombarded surface, with a power law increase in surface roughness. In the present study of ripple evolution by 60 keV argon bombardment on silicon at a 60° angle of ion incidence, even at early stage of sputtering the aspect ratios of ripple patterns are large, which implies development of large slopes on the surface. This highly undulating surface grows due to ion bombardment under the dominant shadowing effect. Neither the BH [15] equation nor the first order nonlinear KS equation advocated by Cuerno *et al* [16] take into account the influence of shadowing. This is probably the reason for the absence of true kinetic roughening in our study as predicted in [16, 34, 19, 20].

3.3. Coarsening of surface ripples on Si by 30 keV Ar ion bombardment

We have seen in the previous section that for 60 keV argon bombardment on silicon at a 60° angle of incidence, the roughness amplitude of the ripple morphology exhibited a power law increase with sputtering time as $W \sim t^\beta$ in contrast to the exponential growth predicted theoretically. This section deals with the dynamics of ripple evolution [8] under 30 keV argon bombardment on silicon at angles of incidence of 60° and 70°. By lowering the ion energy, the amplitude of ripples is decreased and the probability of occurrence of shadowing at early times can be reduced. Under these conditions, we can test the validity of the exponential growth predicted by the theory for the ripple amplitude [15]. The morphology of the ion bombarded surface at different stages of bombardment is presented in figures 7(a)–(c) for $\theta = 60°$ and in figures 7(d)–(f) for $\theta = 70°$. For both angles of incidence, the quasiperiodic ripple patterns developed on the surface at early times are shown in figures 7(a) and (d). The morphological evolution in this case is similar to that observed for 60 keV Ar ion induced rippling at 60° except for the fact that the spatial periodicity is destroyed more quickly for $\theta = 70°$ than for $\theta = 60°$. Figure 8 shows the behavior of roughness amplitude W and ripple wavelength l, as determined from AFM data, with sputtering time.

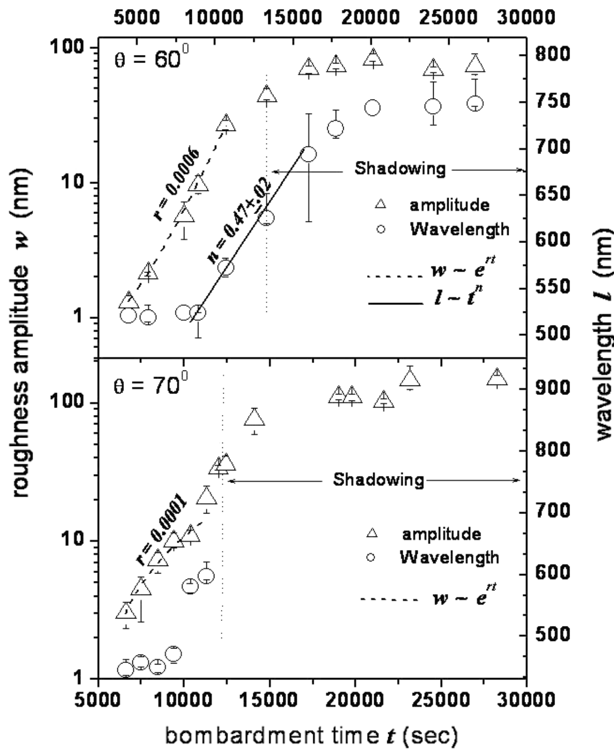

Figure 8. The ripple wavelength l and the surface roughness amplitude w as a function of bombardment time for ion incidence angles 60° (upper figure) and 70° (lower figure).

From the evolution of roughness amplitude in figure 8, we notice that for sputtering times of 4000–13 300 s, when the shadowing effect is absent, the amplitude increases exponentially with sputtering time as $W \sim \exp(rt)$, with the fitting coefficient (growth rate) $r = 6.0 \times 10^{-4}$ s^{-1}. The shadowing regime starts after a sputtering time of ~13 300 s and the roughness amplitude W remains practically constant for further sputtering. On the other hand, the wavelength l remains almost constant for an initial sputtering time of ~4000–9000 s and then grows following a power law dependence $l \sim t^n$ with the exponent $n = 0.47 \pm 0.02$. With the dominance of shadowing beyond ~13 300 s, the wavelength coarsening slows down and finally becomes nearly saturated.

The system correlation length ζ and the ratio of system correlation length with experimentally observed ripple wavelength l are shown in table 2. The lowest sputtering time 4450 s shown in table 2 is within the time regime where the wavelength stays constant and the roughness amplitude varies exponentially. Here the system correlation length ζ and the ratio $\zeta{:}l$ are smaller than those found for the low sputtering time regime at 60 keV ion bombardment (table 1 of section 3.2). This fact indicates a less regular periodic pattern compared to the pattern developed by 60 keV ion bombardment. This is consistent with the observation at this early sputtering time of a surface topography that consists of relatively flat regions coexisting with small amplitude ripple patterned zones, as can be seen from the AFM image in figure 7(a).

Table 2. The lateral correlation lengths and system correlation lengths calculated from AFM images for 30 keV Ar bombardment on Si at $\theta = 60°$ and flux = 18 μA cm^{-2}.

Ion fluence (ions cm^{-2})	time (s)	ξ_x (nm)	ξ_y (nm)	ζ (nm)	$\zeta{:}l$
5×10^{17}	4 450	112	560	431	1.13
1.5×10^{18}	13 300	122	717	592	1.08
2.7×10^{18}	24 000	207	440	438	0.66

For ripple evolution at $\theta = 70°$, in the absence of shadowing, the ripple roughness amplitude grows exponentially with sputtering time. However, the growth rate r is found to be 1.0×10^{-4} s^{-1}, lower than the growth rate at $\theta = 60°$. The shadowing regime also starts earlier than that of $\theta = 60°$, after a sputtering time of ~11 000 s as marked on figure 8. The morphology corresponding to the presence of shadowing effects is represented in figure 7(b). Ripple wavelength l remains constant up to a sputtering time of ~8000 s. The duration of the coarsening process is much shorter than that observed for $\theta = 60°$. Besides, a regular wavelength cannot be defined due to the fast destruction of the ripple pattern after a sputtering time of ~11 000 s.

To study the coarsening of the ripple pattern, apart from checking the increase of l with t, one can also plot the reciprocal of wavelength (l), i.e. the wavevector ($k = 2\pi/l$), versus bombardment time (t). In this plot, it is interesting to look for an offset exponential decay behavior of k with t, as found in the work of Brown *et al* [46]. Following a similar method, we also plotted our data for the rippling on a Si(100) surface generated with 30 keV Ar^+ impinging at a 60° angle of ion incidence, as shown in figure 9. In this figure k represents the experimentally derived wavevector (similar to the apparent wavevector q_{app} in [46]) for the parallel mode ripple observed in our case, which is different from the maximally unstable wavevector k^* predicted by the theory. We see that only the middle portion of the data of figure 9 could be fitted reasonably well with an offset exponential decay function of the form $k = y_0 + \Lambda \exp(-t/\tau)$, where y_0, τ and Λ are fitting parameters with the fitted values being 0.007, 11246 and 0.1163, respectively. At $t = 0$, $k(0) = y_0 + \Lambda$ is characteristic of ripple evolution at a particular temperature, i.e. equivalent to k^*. However, the k values of the data of Brown *et al* [46] could be well fitted with such an empirical exponential decay function for the entire sputtering time for the rippling on Si(111) with 500 eV Ar^+ ions incident at 60° in the temperature region 600–750 °C.

It is difficult to say at this moment whether part of the wavelength coarsening observed before shadowing can be attributed to the contribution of the $\lambda_{ij}^{(2)}$ nonlinearities present in equation (6) of GCC model [21]. This is because the exact expression of $\lambda_{ij}^{(2)}$ and other coefficients of equation (6) in terms of experimental parameters is not known. However, part of the coarsening process, including saturation after shadowing effects, cannot be compared with the GCC model, as the small slope approximation of the model breaks down under the shadowing condition.

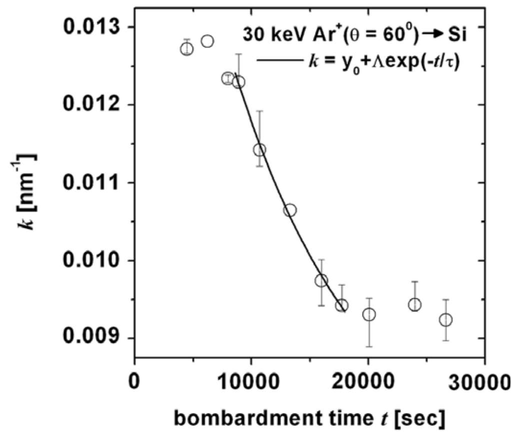

Figure 9. The ripple wavevector $k = 2\pi/l$ as a function of bombardment time for 30 keV ion bombardment at a 60° angle of incidence. The line is a fitted to the experimental data using an offset exponential decay function, $k = y_0 + \Lambda \exp(-t/\tau)$.

3.4. A brief comparison of the Si surface ripples obtained at 60 and 30 keV Ar ion bombardment with some recent experimental works

A comparison of our results for 60 keV Ar ion induced ripples on Si (for a 60° angle of ion incidence) with those obtained for 30 keV Ar^+ sputtered ripples reveals some interesting points. (1) Lowering the ion beam energy from 60 to 30 keV delays the ripple initiation time. (2) Lowering the ion beam energy delays the time of operation of shadowing in the ripple dynamics. (3) For prolonged sputtering the shadowing process slows down the growth of ripple wavelength and amplitude showing a crossover to smaller values of exponents for 60 keV rippling while more or less saturation of the wavelength and amplitude occurs for 30 keV rippling. It is interesting to note that using a Xe ion energy of 10 keV for 60° ion incidence Zhang *et al* [47] showed that the ripple pattern on Si can be formed at threshold ion fluence values as low as 7×10^{15} ions cm^{-2}, which is two orders of magnitude smaller than our results presented here. On the other hand, Katharria *et al* [48] reported ripples on Si by 100 keV Ar^+ at 60° ion incidence at a threshold fluence of 3.5×10^{17}, which is close to our results.

The early time ripple dynamics induced by both 30 and 60 keV Ar^+ beams can be described by the linear continuum model. However, to describe the intermediate and late stage dynamics covering wavelength coarsening, nonlinearity based continuum models should be applied up to around 30 keV ion sputtering. In this sense, ours are the first experimental results that probably give a hint about the upper limit of the energy of ion beam rippling for applying the recently developed new type of nonlinear continuum model (GCC model). Further, the present results show that ordering in the ripple pattern is quickly destroyed at 30 keV (as is evident from the auto-correlation image embedded in each of the AFM images of figure 7) for a 70° angle of ion incidence compared to the case of 60°. It is worth mentioning that recent work of Ziberi *et al* [49] with low energy ($\leqslant$2 keV) noble gas ion bombardment on a Si surface reported ripple patterning for which the ordering improved with sputtering time but without coarsening of the ripple wavelength, which is contrary to the present results. On the other hand, order enhancement of self-organized Si nanodots produced with similar low keV (1.2 keV) Ar ions in a normally incident beam occurred with sputtering time, along with coarsening of the nanopattern wavelength as reported by Gago *et al* [50]. In all these studies [49, 50], due to the absence of shadowing the features of the observed pattern dynamics could be explained well in the light of continuum models.

3.5. Ion energy dependence of ripple wavelength

The study of the dependence of the pattern wavelength (l) with the ion energy (E) is important as it can be used to further test the consistency of the experimental erosion behavior with the assumptions of Sigmund's theory [28], which is the basis of the different continuum models.

For the medium ion energy experiments, the energy range (50–140 keV) sampled in our case is wider due to the use of ion implanters. Therefore, the assessment of the quantitative dependence between l and E becomes more reliable. The ion induced ESD process predicts [16] an increase of ripple wavelength with ion energy as $l \sim E$, but the thermally activated surface diffusion process [15], dominating at high temperature, predicts a reduction of l with increasing E ($l \sim E^{-1/2}$). An increase of l with E has been observed experimentally in several cases [51–53] for rippling processes at room temperature. Direct observation of decreasing l with increasing E has been reported recently by Brown and Erlebacher [54] for low energy (250–1200 eV) Ar^+ sputtered Si(111) at elevated temperature (500–750 °C). So the study of the ion energy dependence of ripple wavelength is important to gain further insight into the type of diffusion prevailing on the ion sputtered surface. For the rippling experiment with a high current ion implanter employed here, ion beam heating of the sample during the irradiation process is unavoidable. However, it can be reduced by simultaneously employing beam scanning, because under these conditions the effective beam intensity on the bombarded spot is reduced as the beam is swept continuously over the sample. With this experimental arrangement, ion beam heating of the sample may be reduced by several hundred °C [55]. So, without employing any external heating of the sample, we investigated the effect of ion beam heating on the variation of ripple wavelength with ion energy just by switching-off the beam scanning.

The results of our study [6] of the ion energy dependence of ripple wavelength are depicted in figure 10. With beam scanning l grows from about 700 to about 1000 nm as the incident ion energy (E) increases from 50 to 140 keV. However, l decays from 600 to about 400 nm with increasing E when the ripple is formed without beam scanning. The power law variation of l with E of the present experiment has exhibited [6] both increasing and decreasing trends with the energy with exponents of 0.45 and −0.56, respectively (figure 10).

When the sample is bombarded with a focused beam without scanning, the beam intensity at the center of the bombarded spot becomes higher than in its peripheral regions, causing a local temperature rise. As the semiconductor sample

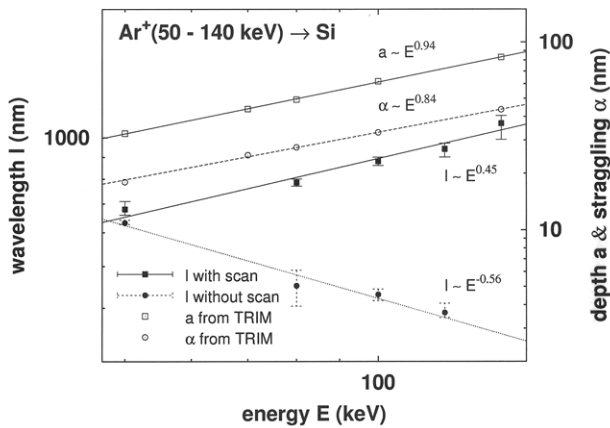

Figure 10. The left scale depicts the variation of the measured wavelengths l as a function of the $^{40}Ar^{+}$ energy and the right scale shows the TRIM calculations for depth a and longitudinal straggling α as a function of ion energy. Power law fits to the wavelengths and TRIM data are inserted into each plot. The error bars of the measured data points have been determined after several repeated experiments, and each data point represents the averages over different regions of the bombarded spot.

in the present case is clamped on a copper block, good thermal contact is not ensured, which favors local temperature rise due to ion beam heating. Under this situation, the rise of temperature, T, from the initial ambient temperature, $T_o = 25\,^{\circ}\mathrm{C}$, at time t (s) of the start of the bombardment can be calculated from the formula [56]

$$t = \int_{T_o}^{T} \frac{Q\kappa\upsilon}{P - (T^4 - T_o^4)}\,\mathrm{d}T, \tag{17}$$

where Q, κ and υ are specific heat (0.836 J g^{-1} °C^{-1}), thickness (0.47 mm) and density (2.32 g cm^{-3}), respectively, of the Si wafer used in the present experiment. The sample temperature thus estimated within 68 s [56] of the start of bombardment was ~800 °C for a beam power $P = 14$ W cm^{-2}, corresponding to the maximum flux (140 μA cm^{-2}) employed in the present case for bombardment at 100 keV. However, this theoretical estimation of temperature is an ideal one and much deviation is expected for real experimental conditions.

It should be kept in mind that the actual surface temperature developed on the bombarded spot during ion bombardment is quite difficult to measure experimentally due to many constraints (one of them being the need to isolate the ion beam from the temperature measuring probe). So, for practical purposes, a rough experimental measurement of the temperature at the back face of the Si wafer using a thermocouple for the above mentioned beam power and energy resulted in 300(±20) °C, much lower than the theoretical value. On the other hand, the temperature of the sample measured following the same procedure with beam scanning was 120(±20) °C. In any case, we have a semi-quantitative idea of the rise of temperature caused by beam induced heating which is drastically reduced by scanning the beam over the sample during bombardment. Consequently, in the present case of bombardment without scanning, thermally activated surface diffusion plays an important role which may be the reason for the observed negative exponent $l \sim E^{-0.56}$. It also seems that the surface temperature profile (STP) generated by an unscanned focused ion beam on the sample has made the thermally activated diffusion process the dominant one. This was not the case even when experiments were performed by increasing the bulk temperature of the sample [2]. However, the negative exponent (−0.45) observed by Brown and Erlebacher [54] for low energy rippling at high temperatures is smaller than that observed in our case for rippling with prominent beam heating.

On the other hand, for irradiation with beam scanning, the effective beam intensity on the bombarded spot is reduced as the beam is swept continuously over the sample. The magnetic beam sweeping system of our implanter uses scan frequencies of 0.51 and 5.3 Hz along the horizontal and vertical direction to maintain beam homogeneity on the irradiated area of the sample. This means that each region of the bombarded spot, with a size close to the beam diameter (about 3 mm), will be exposed to the ion beam after every few seconds only, which is much less than the time required to reach the maximum equilibrium temperature due to beam heating. Under beam scanning conditions, promotion of surface diffusion of thermal origin will be hampered and ion induced surface diffusion will be the main relaxation process. In this case, an increase of l with E, as observed in our data (figure 10), can be expected. However, the experimental results very often show a power law increase of ripple wavelength with energy of the type $l \sim E^n$ with different values of the exponents, $0 < n \leqslant 1$, depending on the ion species for rippling on Si surface [44, 49].

From the positive power law exponent (n) of the $l \sim E^n$ relationship it is possible to determine the shape of the distribution of the deposited energy density in the near surface region induced by the ion collision cascades. For instance, for the case of ripple topography formation on Ar bombarded graphite in the 2–50 keV energy region Habenicht *et al* [52] obtained a power law relation $l(E) \sim E^n$ ($n = 0.95$), while the depth of energy deposition (a) and longitudinal straggling (α) scale with ion energy implying an energy-independent lateral spread of the damage cascade. However, we obtained a much lower value of the exponent ($n = 0.45$) with beam scanning while both depth (a) and longitudinal spread (α) are linear with energy, as obtained exponents from TRIM calculations [57] are close to unity (see figure 10). A lower exponent ($n \ll 1$) is an indication of the change in the lateral spread of the damage cascade with ion energy for the energy region selected in the present experimental situation.

4. Compositional heterogeneity of medium energy Ar ion induced ripples in Si

To confirm the presence of Ar and the spatial inhomogeneities [24] of Ar atoms on the rippled surface of Si we performed elemental mapping and line scans using energy dispersive x-ray spectrometry (EDS) attached in a scanning electron microscope (SEM). The main results of this study [24] reveal

that maxima of Ar intensity are not located at the peaks of ripples but rather towards the middle part of the front slope (facing the ion beam) of the ripples generated under shadowing conditions (for a fluence of 10^{18} ions cm^{-2}). The spatial extension of the Ar rich phase occupies about 40% and 50% of the wavelength of the ripples produced at the corresponding dose. Also we found that the relative Ar concentration varies from about 1 to 4 at.% as one probes from bottom to top along the front slope of ripples, implying that the upward part of the front slopes are Ar rich and valleys are Ar deficient. This variation of the concentration level along the front slope is found to remain almost constant for a rippled surface generated under the ion fluences ranging from 10^{18} to 1.5×10^{18} ions cm^{-2}. This fact implies that a steady state or saturation condition is reached when the concentration of implanted atoms remains constant, even with further bombardment. The experimentally observed compositional heterogeneity [24] between the two faces of the ripples agrees reasonably well with the well known Monte Carlo ion simulator TRIM based theoretical calculations.

5. Structural investigation of keV Ar ion induced surface ripples in Si

If the sputter induced ripple pattern has to be used for nanoscale wire formation, as proposed in a recent paper [25], the knowledge of the microstructure underlying the ripple morphology is necessary in terms of device performance. From a theoretical point of view also, it is essential to know the exact depth of amorphization to properly understand the surface relaxation process. Although damage structures of the low energy ion induced nanopatterned morphology on semiconductor surfaces like Si or GaSb have been studied in a few cases [10, 9, 49] using XTEM, there are to our knowledge no previous studies of the microscopic damage structure of the medium keV heavy ion induced ripple features. Here we will focus on XTEM investigation [23, 26] of the ripples produced following Ar ion (30–120 keV) bombardment of Si. We also used the grazing incidence x-ray diffraction (GIXRD) technique [58] with a synchrotron source for structural analysis of Si surface ripples, but the details of those experiments will be discussed by our colleague in this issue.

Representative XTEM images of ripple patterns generated on an amorphous Si (a-Si) sample after 60 keV $^{40}Ar^{+}$ bombardment at a 60° angle of incidence for a fluence of 1×10^{18} ions cm^{-2} are displayed in figure 11. The sinusoidal-shaped wave patterns of the surface ripples are distinct in the low magnification XTEM image of figure 11(a). The outer surface layer of the irradiated samples shows TEM contrast typical of an amorphous phase, which is separated by a thin line of dark contrast from the crystalline bulk phase. Interestingly, the amorphous layer on the front slope (the side facing the ion beam) is slightly thicker (about 145 nm) than that (73 nm) on the rear slope. The variation in the penetration depth of the ions, caused by the different local angles of incidence, on the surface of the two slopes with the wave morphology (see figure 2) seems to be responsible for the variation in the thickness of the outer amorphous layer. Careful inspection of

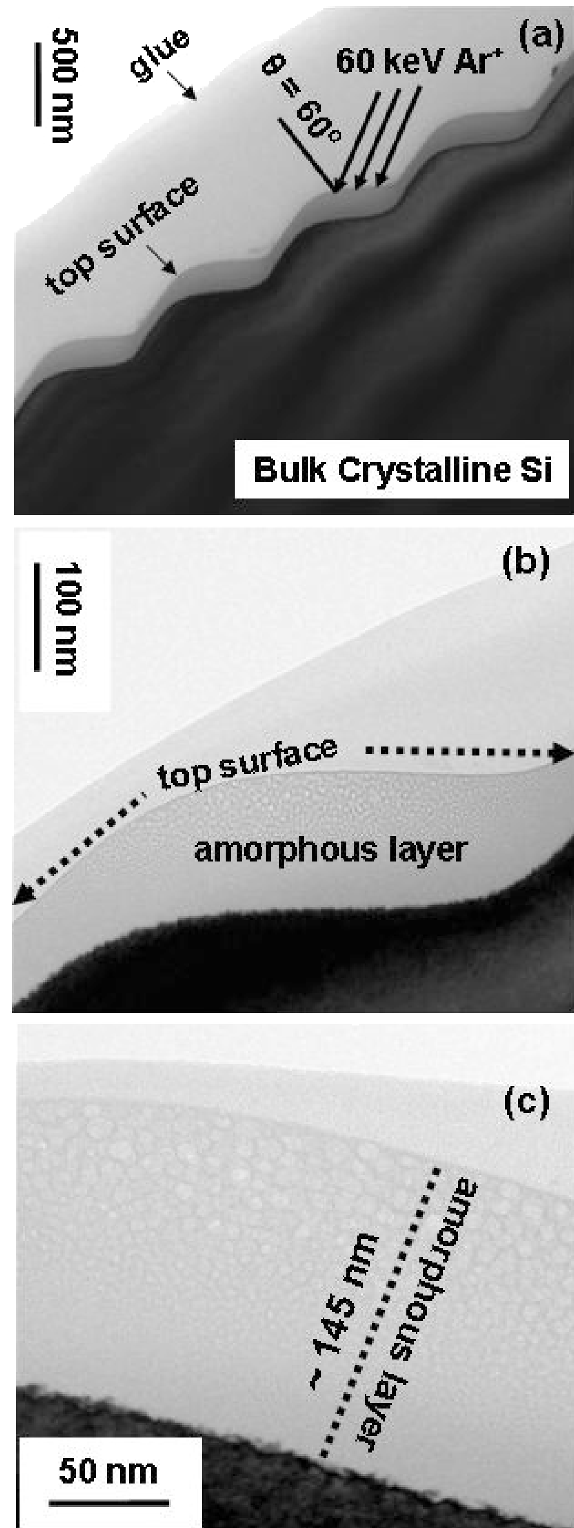

Figure 11. Cross-sectional transmission electron microscopy (XTEM) of a Si surface after 60 keV Ar^{+} bombardment at $\theta_{ion} = 60°$.

the XTEM image of figure 11(c) reveals cavities or porous-like features with an average diameter of 6 nm within the amorphous matrix at the front slope of the ripples. Such features are not prominent on the rear slope, which can be

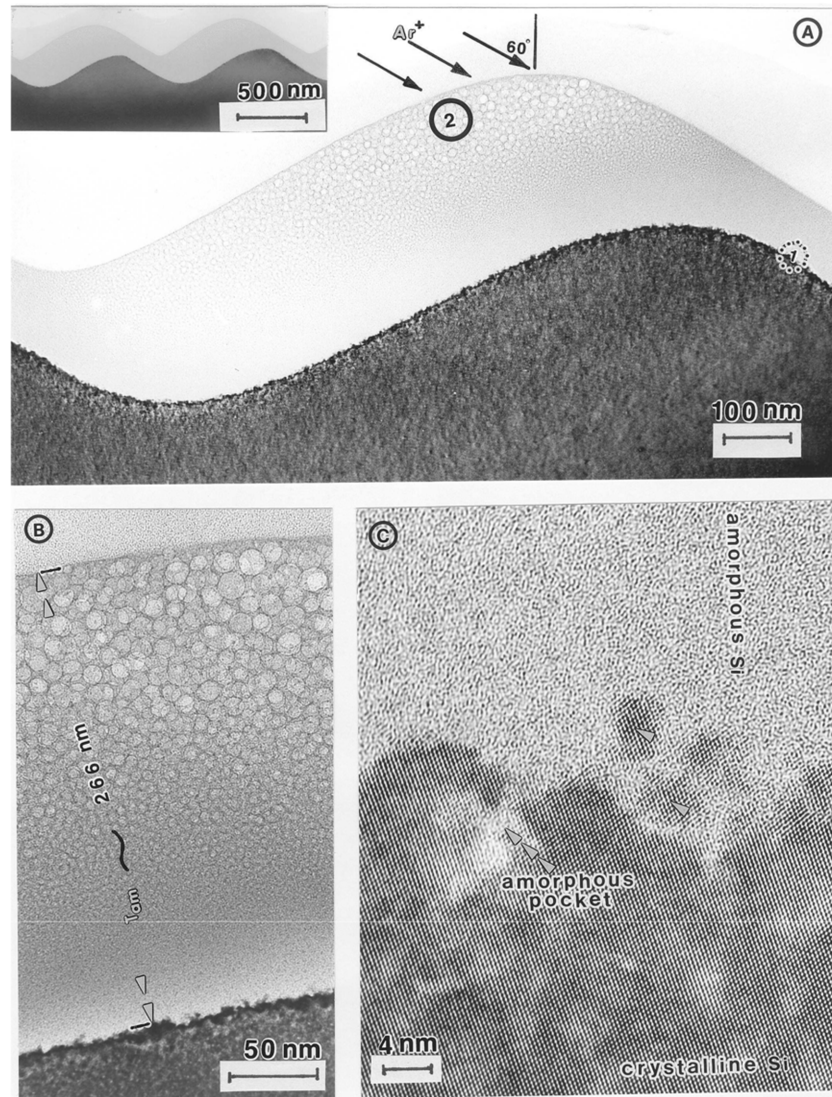

Figure 12. Cross-sectional TEM image of the Si surface sputtered with a 120 keV $^{40}Ar^{+}$ beam. (A) Medium magnification image of an individual wave. Inset: low magnification image. (B) High magnification image from the encircled region 2 of the wave from panel (A). (C) HRTEM image of the encircled region 1 of the wave cross-section of panel (A). Nanocrystallites on the amorphous side of the a/c interface are indicated by arrowheads.

seen from figure 11(b). The accumulation of Ar atoms on the front slope of the ripples was shown in the previous section. The presence of Ar bubbles in the amorphous phase of the as-implanted Si has been reported [59, 60] in a wide energy region (5–150 keV) even in the moderate dose range 10^{15}–10^{16} ions cm^{-2}. For the high dose of 10^{18} ions cm^{-2} employed in the present case, most of the cavities are thus believed to be filled with Ar gas and will be called Ar bubbles hereafter. The calculated areal density of bubbles from the analysis of the TEM micrographs turns out to be in the range (5–11) $\times$ 10^{11} cm^{-2} within the amorphous layer of the front slope. However, it should be mentioned that for high dose keV bombardment, the implanted Ar is expected to be present both atomically dispersed and in the form of bubbles [61].

From the extensive XTEM based structural analysis we also observe that for the fixed ion dose employed here, the thickness of the amorphous surface layer of ripples increases with the energy of the bombarding ion as is clear from the XTEM micrographs of Si ripples induced by 120 keV Ar bombardment (figure 12). The maximum bubble diameter is ~16 nm at 120 keV bombardment, exhibiting an increasing trend in bubble size with ion energy. The smallest detectable size of the bubbles observed in the present experiment is ~3 nm.

5.1. Ripple structure versus luminescence property of silicon

Bulk crystalline silicon (c-Si) has poor light emitting properties due to its indirect band gap. However, it has been established [62, 63] that porous silicon (po-Si) obtained by electrochemical dissolution of Si can have luminescence in broad spectral bands from the visible region to infra-red (IR). This is because po-Si is believed to be composed of nanocrystallites of typical dimension 2–3 nm, which due to

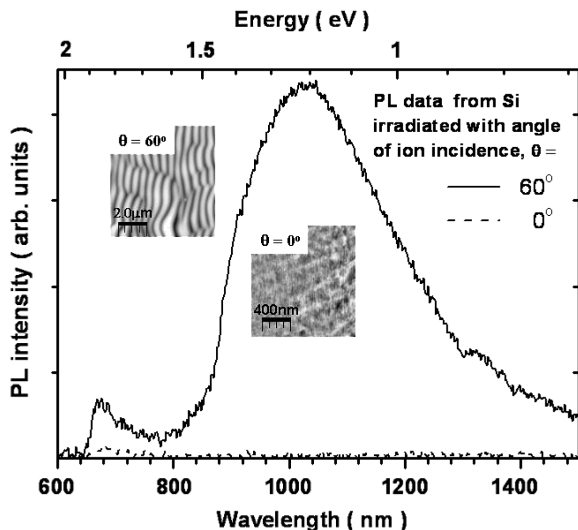

Figure 13. Room temperature photoluminescence spectra from the rippled surface of Si generated after 60 keV $^{40}Ar^{+}$ bombardment at a 60° angle of ion incidence and from a random rough surface produced at normal (0° angle of ion incidence) bombardment. The AFM images of the bombarded Si surfaces for the respective angles of ion incidence are shown in insets. The ion fluence for each of the angles of ion incidence was 1×10^{18} ions cm^{-2}.

quantum size effects [64] permit light emission far above the band gap of bulk Si. However, the chemical route to synthesize po-Si is not well controllable and it is not free of contamination because of air exposure.

An alternative way [65] to make po-Si has been suggested through helium (He) implantation in c-Si at RT followed by annealing up to about 1000 K, leading to bubbles/cavities in the implanted region. Following such prescription a porous structure needed for potential light emission is not as readily achievable by He implantation as the subsequent implantation literature [65–67] might suggest. However, varying the implantation parameters may still lead to such materials, as pointed out by Siegele *et al* [67]. As depicted in figure 13, we have observed [26] room temperature (RT) visible and infra-red (IR) photoluminescence (PL) bands peaked around 680 and 1020 nm, respectively, from a silicon (Si) surface amorphized and patterned with ripples by 60 keV Ar^{+} bombardment at a 60° angle of ion incidence. However, the Si surface amorphized but not patterned under normal bombardment (0° angle of ion incidence) conditions shows a drastic reduction in the intensity of the visible PL along with the complete suppression of IR emission.

Let us discuss whether a correlation exists between the observed PL emission and the structure of the argon bubble containing the a-Si phase found in our high dose argon implanted Si samples. The average size of the a-Si walls in between the bubbles from the present TEM data is estimated to be ∼3 nm, which is comparable to the average radius of the bubbles observed within the amorphous layer of the rippled sample. The size of this a-Si nanostructure agrees well with the typical size (3–5 nm) of the reported [68] visible PL emitting a-Si nanoparticles. So, our experiment gives direct evidence of a highly confined a-Si nanostructure showing visible PL. Obviously, the large size of ∼5–6 nm of the isolated a-Si structures resulted in the normally bombarded sample of the present case not being favorable for visible PL emission.

6. Medium energy ion induced ripple evolution in binary semiconductors

As far as applications are concerned, GaAs is considered to be one of the important III–V binary semiconductor materials for electronic and optical applications. Although these semiconductors are easily amorphized by ion bombardment, like the monoelemental semiconductors, the preferential sputtering of one of the constituents of the III–V binary semiconductors may have an important role in ion induced pattern formation. This issue is not considered in the theoretical models. It is worth mentioning that although results of rippling induced by low energy inert gas ion bombardment are reported sporadically, to the best of our knowledge there have been no medium energy ion induced patterning experiments.

6.1. Ripple morphology on GaAs

The results [69] for the evolution of GaAs surfaces subjected to 60 keV Ar^{+} ion bombardment at a 60° angle of ion incidence (at a flux of 25 μA cm^{-2}) as a function of ion fluence are shown in the AFM images of figures 14(a)–(f).

At a dose of 1×10^{17} ions cm^{-2}, no visible feature has appeared except for the roughening of the surface. At a dose of 2×10^{17} ions cm^{-2}, dots are formed on the ripples, which are not sharp enough to give a clear wave-like feature. However, a tendency to form ripples is evident in the images. As seen in the AFM images, the dots are decorated on the crest of the ripples in the fluence range between 2×10^{17} and 1×10^{18} ions cm^{-2} with the dot diameters varying between 120 and 220 nm. Also a maximum number density of dots of $\sim 6 \times 10^{8}$ cm^{-2} is observed at a dose of 5×10^{17} ions cm^{-2} in the present experiment. Such a value of the number density generated for our off-normally incident 60 keV Ar^{+} bombarded GaAs surface is smaller than that observed by Facsko *et al* [9] for a normally incident low energy Ar^{+} sputtered GaSb surface. The dots along with ripples are observed up to a dose of about 1×10^{18} ions cm^{-2}. However, at a dose of 3×10^{18} ions cm^{-2} only ripples without any dots are seen all over the bombarded region, the wavelength of the ripples being about 1150 nm. The ripples are oriented along the perpendicular direction to the projection of the ion beam on the surface, consistent with the BH model [15].

Figure 15 shows the rms roughness (w) as a function of ion dose. The early stage roughness data have been fitted with an exponential function of the form $w \propto \exp(\phi/\phi_0)$ (with a fitting parameter $\phi_0 = 2.44 \times 10^{17}$), whereas the roughness data at the late stage, i.e. in the high fluence regime of the plot (figure 15), have been fitted with the function $w \propto \phi^{\mu}$ with the fitting parameter $\mu = 0.088$.

The evolution of the topography in the form of islands or dots can be explained in the light of preferential sputtering of As in the low dose regime [70]. Consequently, the surface

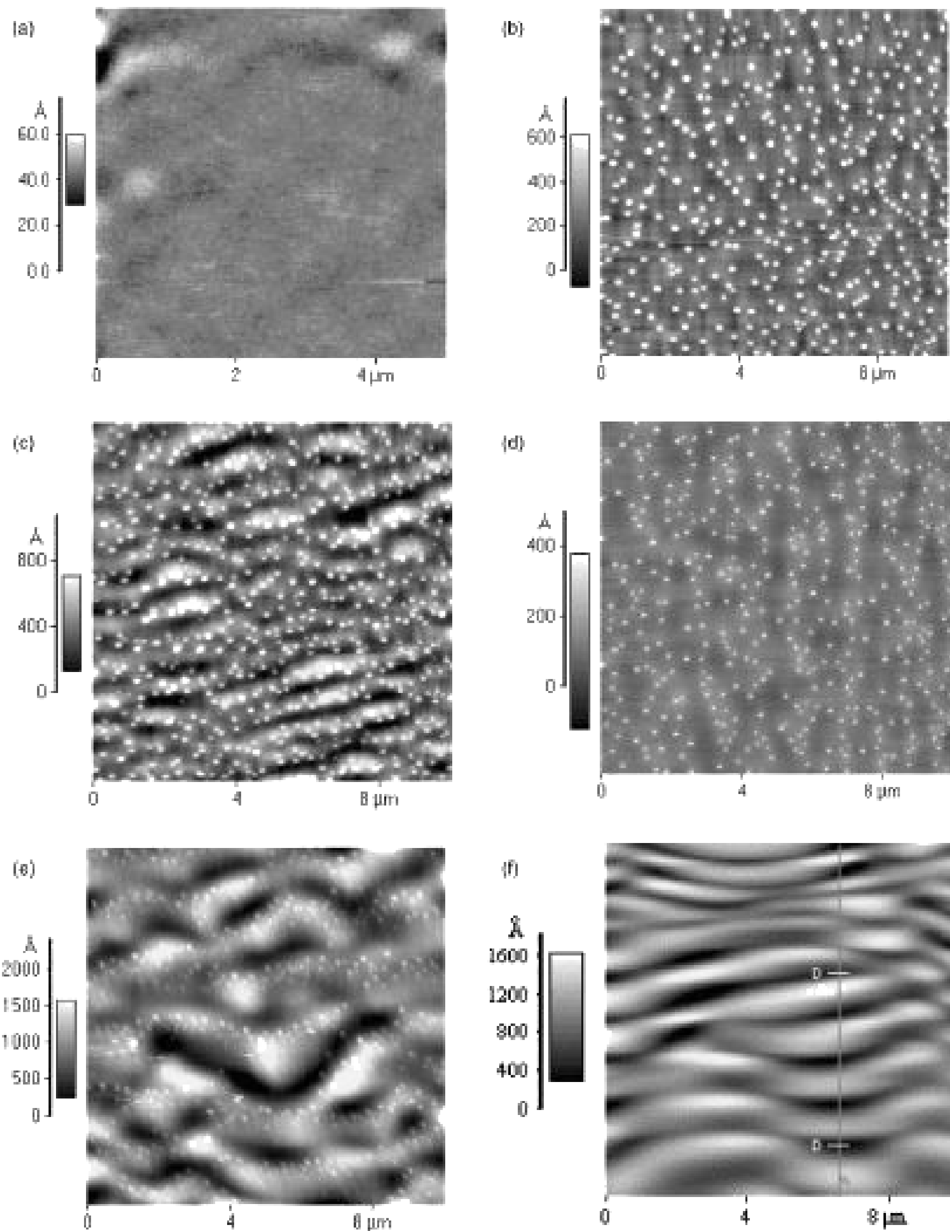

Figure 14. Evolution of topography on GaAs bombarded by 60 keV $^{40}Ar^{+}$ at an angle of 60° with respect to the surface normal. The sequence of AFM pictures shows the dose dependence of topography formation. The bombardment doses are: (a) 1×10^{17} ions cm^{-2}, (b) 2×10^{17} ions cm^{-2}, (c) 5×10^{17} ions cm^{-2}, (d) 7×10^{17} ions cm^{-2}, (e) 1×10^{18} ions cm^{-2} and (f) 3×10^{18} ions cm^{-2}.

is enriched by Ga atoms, and because of enhanced diffusion these Ga atoms agglomerate into Ga islands/dots [70]. This explanation can be substantiated by the results of Facsko *et al* [9] in the case of dot formation for a low energy Ar^{+} sputtered GaSb surface, where using Auger electron spectroscopy (AES) analysis they found enrichment of Ga by 30 at%. In the case of dot formation on a low energy Ar sputtered InP surface, Frost *et al* [11] and Chini *et al* [71] also observed that In enrichment and agglomeration are the determining factors for the dot morphology. Kahng *et al* [18] showed that regular ordered patterns of dots are obtained only at the transition between linear and nonlinear regimes and the transition time is dependent on ion energy and flux. Then, in the present experiment, the irregularity in the distribution of dots observed below the transition time mentioned above seems to be consistent with the prediction of Kahng *et al* [18].

7. Critical issues concerning the instrumentation and experimental conditions

7.1. Need for an ion implanter

The experimental results published so far in the literature on ion beam sputtered (IBS) patterning are based on three types of ion beam systems: (1) a broad beam ion source (e.g. a Kauffman type ion source) based machine; (2) an implanter type machine, and (3) a focused ion beam (FIB) based machine. From the point of view of construction,

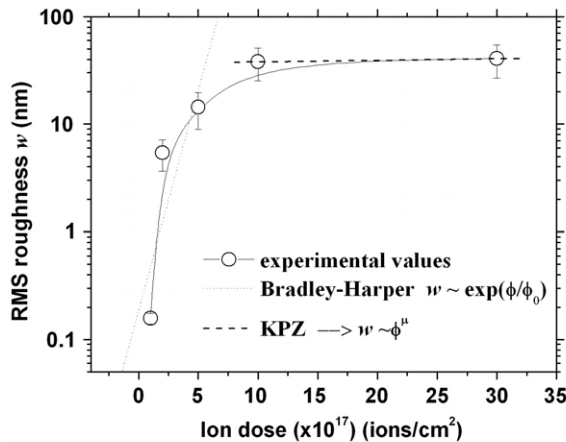

Figure 15. Showing the RMS roughness as a function of ion fluence on GaAs undergoing a bombardment of 60 keV $^{40}Ar^{+}$ at 60° angle.

broad beam based machines are simple and easy to handle but very often suffer from a lack of mass selection, the inability to deliver different kinds of beam species, improper beam collimation and the lack of a variable beam flux and energy, all of which degrade the beam quality. Consequently, morphological features generated on solid surfaces using broad beam ion sources are not always reproducible.

On the other hand, most ion implanter machines use sector magnets. Thus, they can deliver mass-selected ion beams, have high ion flux variabilities from nA cm^{-2} to mA cm^{-2}, and also have ion energy variability. Implanters are usually designed with electrostatic or magnetic x–y beam sweeping systems to ensure homogeneous bombardment on a surface. More importantly, the irradiation chambers of the implanters are equipped with various beam diagnostic components, such as a beam profile monitor and a Faraday cup arrangement for the suppression of secondary electrons caused by the impact of the ions on the target surface. As a result, knowledge of the beam spot size and true ion current ensures accurate information regarding fluence and flux measurement that is not always properly achieved while using a low energy broad beam ion source based machine.

While constructing the theoretical models of the ion induced ripple morphology, it is assumed that the solid surface under consideration is bombarded by a well defined energetic ion beam of a particular mass with uniform ion flux and that homogeneous irradiation is maintained over a region of the surface area of interest. Moreover, the various parameters of the ripple morphology, such as wavelength and amplitude, depend on the mass, energy, fluence (dose) and current density (flux) of the projectile ion and the mass of the target material as well as the temperature of the sample during irradiation/sputtering. So, implanters offer unique opportunities to study rippling processes with much more control on the ion beam parameters than broad beam based machines. Consequently, the resulting ripple topography data generated with a implanter are ideally suited for theoretical comparison. Alternatively, implanters are also the ideal ion beam machine for performing new experiments to test the predictions of theoretical models.

7.2. Merits of broad beam based machines

Because of their constructional features, a high beam flux can be obtained from a broad beam ion source, implying that a patterned morphology can be generated on a large area (several square inches) of a sample within a short time using a low energy system. Moreover, broad beam based machines are very compact and cheap. So, from a technological point of view, the use of a low energy broad beam ion source based machine may be advantageous [9, 10] for mass production of patterned surfaces. FIB systems offer a very high degree of control over patterning but the limitation lies in their ability to pattern over a surface of very small area (typical several 100 μm^2). Also FIB systems are costly, very sophisticated and require time-consuming maintenance. Also, most of the FIB systems deliver a single ion species, namely the Ga ion which is chemically active. Thus, as the formation of a chemical compound depends on the surface of the target, the nature of the surface cannot be ignored, and consequently the role of chemical sputtering on the growth of ripple pattern cannot be ignored. Therefore, whether such ripple data [3, 72] can be discussed with continuum models in the light of Sigmund's theory of sputtering remains an open question.

7.3. Sources of impurities

The probability of the ion bean hitting the apertures/diaphragms or different components of the target chamber at off-normal bombardment becomes high. As a consequence, sputtered particles from these parts of the chamber act as a source of impurities. Such surface impurities and others originating due to mechanical or chemical treatment are thought to be one of the causes of the formation of a cone-like topography [73, 74] on ion bombarded surfaces. The possibility of superposition of such features on the ripple morphology should be avoided if consistent ripple data are to be used for theoretical comparison. Use of a material with a low sputtering yield and high melting point, such as molybdenum, should be as part of the components of the chamber where the probability of hitting the beam is high. Quite recently, Sánchez-García *et al* [75] reported that, apart from the metal impurities (like Mo) generated in the target/sputtering chamber, the internal chamber of the ion source itself may be an unavoidable source of metal impurities (like Fe) to affect the ion beam patterned nanodot/nanohole morphology on Si(100).

The properties of a target surface may also change during an irradiation experiment due to contamination by background gas in the vacuum. The use of ultra high vacuum (UHV) in the irradiation chamber is preferable, in order to minimize the impurities originating from the residual gases. However, most of the ion induced rippling experiments are performed in the high vacuum range (10^{-5}–10^{-7} mbar) using diffusion pumps or turbo pumps. The possibility of hydrocarbon contamination coming out from the backstreaming of diffusion pump oil (when no traps are used) is a major source of impurities for diffusion pump based vacuum systems and also for turbo pump based system where rotary pumps are used as a backing pump instead of diaphragm pumps. Contamination by hydrocarbon impurities can easily be identified with the naked eye by

the presence of a bluish layer (originating from the cracking of hydrocarbon molecules by the incident ion beam) on the sample surface after the bombardment is over. Even at a background vacuum of 2×10^{-9} mbar, the main impurities that contaminate the target surface are oxygen together with water vapor and nitrogen [76]. So, for all practical purposes, as a (too) crude rule of thumb, the bombarded surface should be maintained at least in a dynamically clean condition as given by the following criterion [70]:

$$Y\phi \gg c_s\delta, \qquad (18)$$

where, Y is the sputtering yield of a target for a particular ion species at a given energy and angle of ion incidence, ϕ is the incident ion flux, c_s is the sticking coefficient, and δ is the background flux, given by [77]

$$\delta = 4.66 \times 10^{22} \left(\frac{P}{\sqrt{MT}}\right), \qquad (19)$$

where P is the pressure in mbar, T is the temperature in K and M is the molecular weight of the impinging gas. For diatomic gases (like oxygen or nitrogen) this number should be multiplied by a factor of 2. Let us now assess the condition of a dynamically clean surface for our results of a rippling experiment on silicon surface reported in this review. The rate of impingement of O_2 molecules from the background gas at 300 K and 10^{-7} mbar pressure is $\sim 9 \times 10^{13}$ molecules cm^{-2} s^{-1} which also represents the maximum number of oxygen adsorbates if the sticking probability c_s is taken to be unity. The ion flux of 1 μA cm^{-2} corresponds to 6.25×10^{12} ions cm^{-2} s^{-1}. Therefore, ion flux in the range 15–200 μA cm^{-2} and a sputtering yield of 7 atoms/ion (sputtering yield is estimated from SRIM [57]) for 60 keV Ar $\rightarrow$ Si at a 60° angle of ion incidence, removes the surface atoms at a rate of (0.66–8.8) $\times 10^{15}$ particles cm^{-2} s^{-1} which clearly satisfies relation (18).

8. Conclusion and outlook

In conclusion, the evolution of ripple morphology induced by medium energy (30–120 keV) argon bombardment on a silicon surface has been extensively investigated by *ex situ* atomic force microscopy (AFM) in ambient conditions. The resultant microstructure has also been studied by cross-sectional transmission electron microscopy (XTEM) as well as energy dispersive x-ray spectrometry (EDS). For short sputtering times, the ripple wavelength remains constant and subsequently increases with time following a power law dependence followed by saturation. The late stage dynamics of ripple patterns induced by medium keV argon ions is dominated by shadowing effects that destroy the long range order of the ripple patterns. The sinusoidal profiles of ripple morphology turn into sawtooth-like/triangular-like profiles giving a faceted morphology. From the comparison of ripple data using a 60 keV argon beam with that of a 30 keV argon beam, we find that the early time ripple dynamics can be described by a linear continuum model with reasonable agreement. To describe the intermediate and late stage dynamics covering wavelength coarsening, the recently proposed nonlinear based continuum model can be applied only qualitatively up to around 30 keV ion sputtering. Elemental mapping and line scans using energy dispersive x-ray spectrometry (EDS) with a scanning electron microscope (SEM) confirmed that subsequent to the inter-peak shadowing of incident ion flux, most of the argon atoms are incorporated around the middle part of the front slope of the ripple facing the ion beam as compared to the rear slope. For ripples generated for Ar ion bombardment of Si with 60° angle of ion incidence, the XTEM results reveal that the front slopes of ion induced ripples have amorphous layers containing bubbles with sizes ranging from about 3 to 15 nm facing the direction of the ion beam. A thinner amorphous layer without bubbles, on the other hand, persists on the rear slope of the ripples. The thickness of the amorphous surface layer as well as the bubble size increase with ion beam energy. The present work also demonstrates that medium energy Ar ion irradiation under rippling conditions may yield a porous-like light emitting amorphous silicon (a-Si) nanostructure.

The experimental studies on the medium energy ion induced rippling process have two important aspects: (1) the effect of geometrical shadowing on the evolution of argon ion induced ripple morphology and (2) inclusion of nanosize bubbles within the amorphous layer of the bombarded silicon. These findings have not been reported extensively in the rippling experiments published so far, usually in the low energy regime, or included in the latest continuum theories for the evolution of patterning on the ion bombarded surface. As a result, we have shown the limitation of the existing theories in explaining some of the features of the dynamics of ion induced pattern formation and we believe our data may provide an important input for theorists in search of refined theoretical models. Another important finding is the observation of nanodot decorated ripples on the surface of ion bombarded binary semiconductors, like GaAs. In fact, so far there are no theoretical models taking into consideration the role of varying composition on nanopatterning by ion beam sputtering for binary semiconductors. In this sense, controlling the nanopatterning on binary semiconductors needs urgent attention. Quite recently, a theoretical formalism [78] has predicted that not only preferential erosion but also compositional modulation can give rise to ripple growth, at least for ion bombarded alloy surfaces. However, no experimental verification has been reported so far in support of this prediction.

From the structural point of view and from the observation of photoluminescence, the bubble containing amorphous phase of the rippled surface offers a unique system for realization of the synthesis of an ion beam induced porous system having optical properties similar to the light emitting porous silicon that has so far been synthesized by an uncontrolled chemical method. The difference in the thickness of the amorphous layer between the two slopes of the ripples along with the presence of the cavities/voids in the ion-beam-facing side of the ripple slope may offer the possibility of decorating it with metal particles having unique optoelectronic properties. From our present study it appears that as the energy of the impinging ions

increases from several hundred eV to few tens of keV the role of implanted atoms become appreciable, causing substantial structural and compositional modifications of the bombarded material. Consequently, not only is the morphology of the surface nanostructures controllable but there is also the possibility of generating embedded nanomaterials through structural and compositional reordering using medium energy heavy inert gas ions.

Acknowledgments

The authors thank Mr S Roy, Mr S Banerjee and Dr D Datta for their help in implantation work and Mr A Das, Mr P Mishra and Professor D Ghose for help in AFM measurements. TKC acknowledges the generous help of Dr A Mücklich of FZD-Rossendorf, Germany and Professors F Okuyama and M Tanemura of Nagoya Institute of Technology, Japan for the TEM measurements. He is also grateful to Professor R Cuerno of Universidad Carlos III de Madrid, Spain, Dr L Vázquez of Instituto de Ciencia de Materiales de Madrid, Spain and Professor U Valbusa of Unitá INFM di Genova, Italy for valuable discussions. Finally, the authors thank Professor M K Sanyal of the Saha Institute for illuminating discussions.

References

[1] Hanley L and Sinott S B 2002 *Surf. Sci.* **500** 500
[2] Carter G and Vishnyakov V 1996 *Phys. Rev.* B **54** 17647
[3] Habenicht S, Lieb K P, Koch J and Wieck A D 2002 *Phys. Rev.* B **65** 115327
[4] Erlebacher J, Aziz M J, Chason E, Sinclair M B and Floro J A 1999 *Phys. Rev. Lett.* **82** 2330
[5] Rusponi S, Costantini G, Boragno C and Valbusa U 1998 *Phys. Rev. Lett.* **81** 2735
[6] Chini T K, Sanyal M K and Bhattacharyya S R 2002 *Phys. Rev.* B **66** 153404
[7] Datta D P and Chini T K 2004 *Phys. Rev.* B **69** 255313
[8] Datta D P and Chini T K 2007 *Phys. Rev.* B **76** 075323
[9] Facsko S, Dekorsy S T, Koerdt C, Trappe C, Kurz H, Vogt A and Hartnagel H L 1999 *Science* **285** 1551
[10] Gago R, Vazquez L, Cuerno R, Varela M, Ballesteros C and Albella J M 2001 *Appl. Phys. Lett.* **78** 3316
[11] Frost F, Schindler A and Bigl F 2000 *Phys. Rev. Lett.* **85** 4116
[12] Moroni R, Sekiba D, Buatier de Mongeot F, Gonella G, Boragno C, Mattera L and Valbusa U 2003 *Phys. Rev. Lett.* **91** 167207
[13] Bisio F, Moroni R, Mongeot de F B, Canepa M and Mattera L 2006 *Appl. Phys. Lett.* **89** 052507
[14] Mele E, Benedetto Di F, Cingolani R, Pisignano D, Toma A, Mongeot de F B, Buzio R, Boragno C, Firpo G, Mussi V and Valbusa U 2005 *Nanotechnology* **16** 2714
[15] Bradley R M and Harper J M E 1988 *J. Vac. Sci. Technol.* A **6** 2390
[16] Cuerno R and Barabási A L 1995 *Phys. Rev. Lett.* **74** 4746
Cuerno R, Makse H A, Tomassone S, Harrington S T and Stanley H E 1995 *Phys. Rev. Lett.* **75** 4464
[17] Barabási A L and Stanley H E 1995 *Fractal Concepts in Surface Growth* (Cambridge: Cambridge University Press)
[18] Kahng B, Jeong H and Barabási A L 2001 *Appl. Phys. Lett.* **78** 805
[19] Makeev M A, Cuerno R and Barabási A L 2002 *Nucl. Instrum. Methods* B **197** 185
[20] Park S, Kahng B, Jeong H and Barabási A L 1999 *Phys. Rev. Lett.* **83** 3486
[21] García J M, Castro M and Cuerno R 2006 *Phys. Rev. Lett.* **96** 086101
[22] Carter G 1999 *J. Appl. Phys.* **85** 455
[23] Chini T K, Okuyama F, Tanemura M and Nordlund K 2003 *Phys. Rev.* B **67** 205403
[24] Datta D P and Chini T K 2005 *Phys. Rev.* B **71** 235308
[25] Kim J, Kahng B and Barabási A L 2002 *Appl. Phys. Lett.* **81** 3654
[26] Chini T K, Datta D P, Facsko S and Mücklich A 2007 *Appl. Phys. Lett.* **92** 101919
[27] Chini T K, Bhattacharyya S R, Ghose D and Basu D 1991 *Japan. J. Appl. Phys.* **30** 2895
[28] Sigmund P 1969 *Phys. Rev.* **184** 383
Sigmund P 1973 *J. Mater. Sci.* **8** 1545
[29] Mullins W W 1959 *J. Appl. Phys.* **30** 77
[30] Herring C 1950 *J. Appl. Phys.* **21** 301
[31] Erlebacher J, Aziz M J, Chason E, Sinclair M B and Floro J A 2000 *J. Vac. Sci. Technol.* A **18** 115
[32] Eklund E A *et al* 1991 *Phys. Rev. Lett.* **67** 1759
[33] Yang H N *et al* 1994 *Phys. Rev.* B **50** 7635
[34] Makeev M A and Barabási A L 1997 *Appl. Phys. Lett.* B **71** 2800
[35] Jayaprakash C, Hayot F and Pandit R 1993 *Phys. Rev. Lett.* **71** 12
[36] Kardar M, Parisi G and Zhang Y-C 1986 *Phys. Rev. Lett.* **56** 899
[37] Castro M, Cuerno R, Vázquez L and Gago R 2005 *Phys. Rev. Lett.* **94** 016102
[38] Aste T and Valbusa U 2004 *Physica* A **332** 548
Aste T and Valbusa U 2005 *New J. Phys.* **7** 122
[39] Umbach C C, Headrick R L and Chan K C 2001 *Phys. Rev. Lett.* **87** 246104
[40] Chini T K, Datta D, Bhattacharyya S R and Sanyal M K 2001 *Appl. Surf. Sci.* **182** 313
[41] Zhao Y, Wang G C and Lu T M 2001 *Characterization of Amorphous and Crystalline RoughSurface: Principle and Applications* (New York: Academic)
[42] Kim J, Cahill D G and Averback R S 2003 *Phys. Rev.* B **67** 045404
[43] Zhao Y P, Yang H N, Wang G C and Lu T M 1998 *Phys. Rev.* B **57** 1922
[44] Vajo J J, Doty R E and Cirlin E H 1996 *J. Vac. Sci. Technol.* A **14** 2709
[45] Wittmaack K 1990 *J. Vac. Sci. Technol.* A **8** 2246
[46] Brown A D, Erlebacher J, Chan W L and Chason E 2005 *Phys. Rev. Lett.* **95** 056101
[47] Zhang K, Rotter F, Uhrmacher M, Ronning C, Hofsäss H and Krauser J 2007 *Surf. Coat. Technol.* **201** 8299
[48] Katharria Y S, Kumar S, Sharna A T and Kanjilal D 2007 *Appl. Surf. Sci.* **253** 6824
[49] Ziberi B, Frost F, Hoche T and Rauschenbach B 2005 *Phys. Rev.* B **72** 235310
[50] Gago R, Vázquez L, Plantevin O, Metzger T H, Muñoz-García J, Cuerno R and Castro M 2006 *Appl. Phys. Lett.* **89** 233101
[51] Datta A, Wu Y R and Wang Y L 2001 *Phys. Rev.* B **63** 125407
[52] Habenicht S, Bolse W, Feldermann H, Geyer U, Hofsäss H, Lieb K P and Roccaforte F 2000 *Europhys. Lett.* **50** 209
[53] Flamm D, Frost F and Hirsch D 2001 *Appl. Surf. Sci.* **179** 95
[54] Brown A D and Erlebacher J 2005 *Phys. Rev.* B **72** 075350
[55] Parry P D 1976 *J. Vac. Sci. Technol.* **13** 622
[56] Dearnaley G, Freeman J H, Nelson R S and Stephen J 1973 *Ion Implantation* (Amsterdam: North-Holland) p 423
[57] available from: www.srim.org
[58] Hazra S, Chini T K, Sanyal M K, Grenzer J and Pietsch U 2004 *Phys. Rev.* B **70** 121307(R)
[59] Revesz P, Wittmer M, Roth J and Mayer J W 1978 *J. Appl. Phys.* **49** 5199

[60] Bangert U, Goodhew P J, Jeynes C and Wilson I H 1986 *J. Phys. D: Appl. Phys.* **589** 19
[61] Filius H A, Vanveen A, Bijkerk K R and Evans J H 1989 *Radiat. Eff. Defects Solids* **108** 1
[62] Canham L T 1990 *Appl. Phys. Lett.* **57** 1046
[63] Kanemitsu Y 1995 *Phys. Rep.* **263** 1
[64] Cullis A G and Canham L T 1991 *Nature* **353** 335
[65] Evans J H, van Veen A and Griffioen C C 1987 *Nucl. Instrum. Methods* B **28** 360
[66] Eaglesham D J, White A E, Feldman L C, Moriya N and Jacobson D C 1993 *Phys. Rev. Lett.* **70** 1643
[67] Siegele R, Weatherly G C, Haugen H K, Lockwood D J and Howe L M 1995 *Appl. Phys. Lett.* **66** 1319
[68] Bustarret E, Sauvaian E and Ligeon M 1997 *Phil. Mag. Lett.* **75** 35
[69] Datta D, Bhattacharyya S R, Chini T K and Sanyal M K 2002 *Nucl. Instrum. Methods* B **193** 596
[70] Malherbe J B 1994 *CRC Crit. Rev. Solid State Phys. Mater. Sci.* **19** 55
[71] Chini T K, Kato J, Tanemura M and Okuyama F 1995 *Nucl. Instrum. Methods* B **95** 313
[72] Alkemade P F A 2006 *Phys. Rev. Lett.* **96** 107602
[73] Kelly R and Auciello O 1980 *Surf. Sci.* **100** 135
[74] Wehner G K 1985 *J. Vac. Sci. Technol.* A **3** 1821
[75] Sánchez-García J A, Vázquez L, Gago R, Redondo-Cubero A, Albella J M and Czigány Zs 2008 *Nanotechnology* **19** 355306
[76] Bhattacharyya S R, Brinkmann U and Hippler R 1999 *Appl. Surf. Sci.* **150** 107
[77] Sze S M 1985 *Semiconductor Devices, Physics and Technology* (New York: Wiley)
[78] Shenoy V B, Chan W L and Chason E 2007 *Phys. Rev. Lett.* **98** 256101